AN ABSTRACT OF THE THESIS OF

DICK C. DUKER for the degree of MASTER OF SCIENCE

in Atmospheric Sciences presented on 23 August 1977

Title: SYNOPTIC INFLUENCES ON THE EVOLUTION OF A SEVERE HAILSTORM ENVIRONMENT

Abstract approved: Redacted for privacy

Two summertime days were investigated, 27 and 28 June 1973, to observe the changes in the environment that led to the severe hailstorm on 28 June in the National Hail Research Experiment (NHRE) network, Colorado. Within the network thermodynamic analyses revealed the 28th to have:

(1) Above-average low-level moisture.

(2) Approximately equal heating as on the 27th.

(3) A lower stability index in the morning than on the previous morning.

(4) A potentially unstable layer at the top of the mixed layer.

The small scale and weakness of an eastward-migrating short wave trough suggested application of a perturbation wind analysis, which showed a vortex moving across the country. Divergence computations at upper levels displayed a divergent region downstream of the

vortex and convergent region upstream. The ascent associated with this upper-level divergence led to release of the potential instability found on the 28th, resulting in severe convective storms within the NHRE network.

Satellite photographs suggest that the short wave trough originated off the Baja California coast, and show the perturbation vortex-associated clouds to move across the U.S. in good agreement with estimated locations of the divergence maximum.

Synoptic Influences on the Evolution of a Severe Hailstorm Environment

by

Dick C. Duker

A THESIS

submitted to

Oregon State University

in partial fulfillment of
the requirements for the
degree of

Master of Science

June 1978

APPROVED

Redacted for privacy

Assistant Professor of Atmospheric Sciences
in charge of major

Redacted for privacy

Chairman of Department of Atmospheric Sciences

Redacted for privacy

Dean of Graduate School

Date thesis is presented August 23, 1977

Typed by A & S Bookkeeping/Typing for Richard C. Duker

ACKNOWLEDGEMENTS

I wish to thank Professor W. Lawrence Gates and Associate Professors Fred W. Decker and Larry J. Mahrt for their contribution in reviewing this thesis.

In particular I would like to thank Assistant Professor David A. Barber for his guidance and assistance, without whose help this thesis would not have been possible.

National Hail Research Experiment (NHRE) data was supplied through the courtesy of the National Center for Atmospheric Research, Boulder, Colorado. This research was sponsored in part by NHRE grant 30-262-9066, and National Science Foundation grant 30-262-1670.

TABLE OF CONTENTS

LIST OF TABLES

LIST OF FIGURES

SYNOPTIC INFLUENCES ON THE EVOLUTION OF A SEVERE HAILSTORM ENVIRONMENT

I. INTRODUCTION

It has long been known that the occurrence of severe convective storms is highly correlated with the large scale synoptic situation. Finley (1890) stated that all "violent local storms" are found in the SE quadrant of cyclones which have developed sufficient instability through above-normal low level moisture and shear-induced upper level dryness. Today we know this is true for the most severe of storms, but there exist many severe convective storms not directly associated with these extratropical cyclones. Summertime advective processes in the Great Plains region of the United States can very often realize large instabilities, which when coupled with a synoptically induced dynamic forcing mechanism, will result in a severe storm. This forcing mechanism is not well understood, and even recent studies of severe convective storms, e.g., Ellrod and Marwitz (1976), gloss over the processes of instability release by use of the nebulous term "triggering mechanism".

The National Weather Service operational definition of a severe convective storm, or severe thunderstorm, is a storm resulting in one or more of the following:

(1) surface winds (sustained or gusts) of 50 kts or greater

(2) a tornado

(3) severe or extreme turbulence

(4) hail with a diameter of 3/4 inch or larger

(NOAA, 1977).

Northeast Colorado has the distinction of having the nation's highest annual number of days with hail (Baldwin, 1973), though most of the hailstorms produce hail smaller than 3/4" and are classified as non-severe. This hail maximum is the result of a sufficient moisture source from the Gulf of Mexico during the spring and summer months, and influences due to the mountainous terrain of the region. Day time mountain slope heating with resultant upslope winds is an important orographic lifting mechanism capable of initiating small-hail storms. The elevated site of the region (>1200 m) reduces the thickness between surface and freezing levels, thereby allowing small hail to reach the ground before melting. Mountain lee waves can also assist the growth of hailstorms by providing upward motions (Booker, 1963). These topographical influences in conjunction with the advection of cyclonic vorticity appear to be instrumental in the production of severe hail-storms in the northeast Colorado region (Foote and Fankhauser, 1973).

Since 1969, a hail suppression study, the National Hail Research Experiment (NHRE), has been in progress in northeast Colorado, sponsored by the National Center for Atmospheric Research (NCAR).

Although this study is primarily interested in hail suppression, the data are also being used to increase our understanding of hailstorms. Mahrt (1975, 1976) has used these data to statistically model the environment on hail days and non-hail days. An equally important use of the data is the case study, which can show the development of a hailstorm environment.

On 28 June 1973, a large storm passed through the hail project area, producing strong surface winds and hail two centimeters in diameter (a severe convective storm). The storm itself has been extensively described by Ellrod and Marwitz (1976), in which they found indications of a mesolow beneath the inflow region of the cloud. This thesis will present the results of a case study of two days, 27 and 28 June 1973, exhibiting the evolution of a severe hailstorm environment through synoptic processes.

II. LITERATURE REVIEW

Convective storms may be described as severe or non-severe. Severe storms have either a single large cell, a supercell, which may persist for several hours, as described by Browning and Ludlam (1962); or multiple cells, each cell having a short lifecycle as depicted by Byers and Braham (1949). Non-severe storms are also composed of one or more cloud cells, but all cells have a Byers and Braham lifecycle.

In their study of thunderstorms, Byers and Braham (1949) describe the three stages of development of a thunderstorm cell. The first stage, the cumulus stage, is characterized by updrafts throughout the cell. The bulk of the updraft is fed by converging low level air, although air may enter the cell from any level. In-cloud temperatures are always warmer than the surrounding air at all levels.

The second stage, or mature stage, begins with the onset of rain. At this time the cloud will usually experience vigorous growth due to an increase of energy through the initiation of the downdraft. This stage has both updrafts and downdrafts, and if present, hail would fall during this stage.

The final stage, the dissipating stage, begins when the updraft disappears. It is characterized by weak downdrafts and light precipitation. Each cell passes through every stage before finally dissipating,

the mean lifetime of the cell being about 30 minutes.

Both non-severe and severe storms have updrafts and downdrafts. In non-severe storms the downdrafts become coincident with the updrafts, eventually destroying the updrafts; while in severe storms the updrafts and downdrafts symbiotically coexist through organization into parallel sloping cores. The remainder of the review will concentrate on the more interesting of these storms, the severe storm.

Severe Convective Storm Types

Severe convective storms have been subdivided into two basic types, the multicell severe storm and the supercell storm. Figure 1 shows an example of a multicell severe storm, the Raymer Hailstorm (Browning et al., 1976). This type of storm usually has three or more cells, each at a different stage of development. As the upwind cell dissipates, a new cell, the "daughter cell", forms downwind of the main cloud at distances up to 30 km from the core of the storm (Browning et al., 1976). These daughter cells quickly merge with the main storm body, thereby insuring the storm's longevity. Since the daughter cells form in advance of the storm, the storm will propogate forward as the rearward cells dissipate. The storm will also be carried along by mid-tropospheric winds. This type of storm will usually persist until it encounters a region of low level cold and/or dry air.

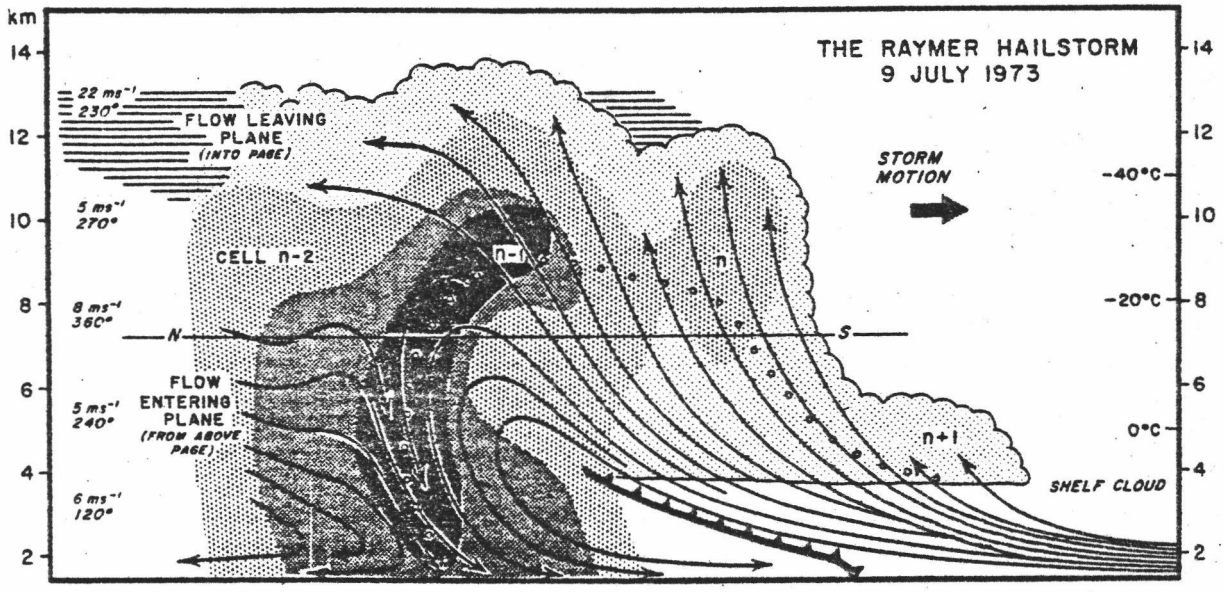

Figure 1. Multicell severe convective storm. Cells n+1 and n are in the cumulus stage, n-1 is in the mature stage, and n-2 is in the dissipating stage. The sloping updraft contributes to the intensity of the storm. Solid lines are streamlines of flow relative to the moving system. The open circles represent the trajectory of a hailstone during its growth from a small droplet at cloud base. Lightly stippled shading represents the extent of the cloud and the three darker grades of stippled shading represent radar reflectivities of 35, 45 and 50dbz. From Browning et al. (1976).

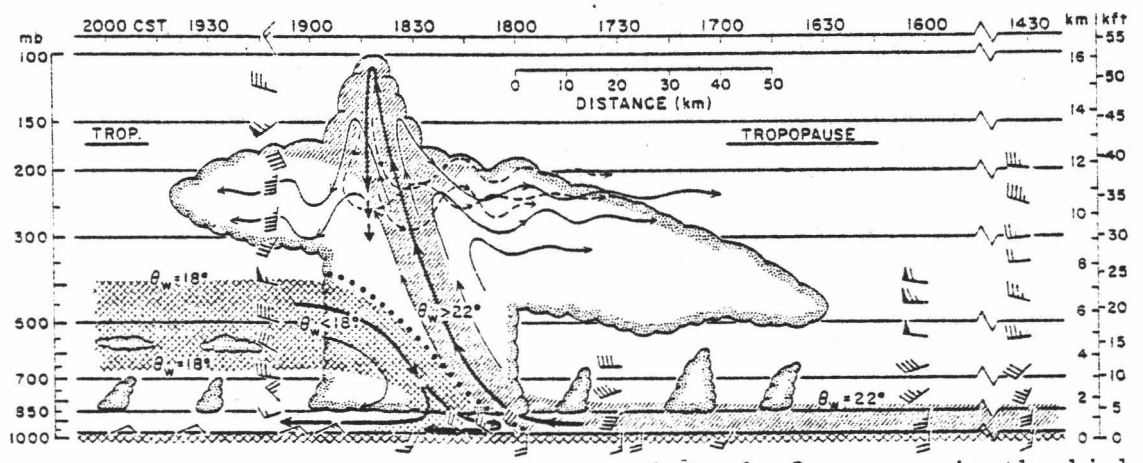

Figure 2. A supercell severe storm. The updraft source is the high θ_w region and the downdraft source is the low θ_w region. Hatching indicates depth of air with θ_w in excess of 22°C, and its probable extent in updraft and upper portion of cloud. Cross-hatching indicates extent of air with θ_w less than 18°C, based on sounding behind storm and on SFC observations. Heavy arrows, axis of main drafts; light arrows, relative streamlines, dashed where air emanates from core of stratospheric tower. From Newton (1966).

The second type of severe convective storm, the supercell storm, has only one cell (Figure 2). Within this cell is a well-organized updraft and downdraft couplet separate from one another, enabling the storm to last several hours. Although comprising a minority of all severe storm cases (Browning et al., 1976), this type of storm has the largest hailstones and strongest winds. Supercell storms may be found isolated or in the midst of multicell storms, but in either case they can usually be identified on radar by a hook echo near the cloud base, or as an echo moving to the right of nearby echoes. This latter phenomenon is a result of the tendency of the supercell storm to propogate to the right of the mid-tropospheric winds while in the intense phase, and with the mid-tropospheric winds otherwise. Marwitz (1972a,b) has shown these storms to be associated with greater vertical wind shear than the multicell type, due to stronger winds in the low levels.

Updrafts

Severe convective storms move approximately at mid-tropospheric wind velocities as a result of strong vertical mixing within the storm. Thus in middle latitudes where wind speeds increase with height, the storms will move faster than the low level air. Relative to the storm, low level air will have a component into the storm. This warm, moist inflowing air is forced to rise by the downdraft-induced high pressure

region under the storm, and once lifted these air parcels will continue to rise due to buoyancy generated from latent heat release. These rising parcels constitute what is known as the updraft. Flights just below the cloud base have shown the updraft air to have high specific humidity and low potential temperature relative to surroundings which could only have originated from near the surface (Marwitz, 1972c; Ellrod and Marwitz, 1976). Updraft speeds are commensurate with horizontal wind speeds, reported values exceeding 25 m sec^{-1} (Marwitz, 1972c).

Foote and Fankhauser (1973) observed that for large, persistent severe storms, the inflow air at cloud base is usually negatively buoyant. This indicates that dynamic forcing rather than thermal forcing must be responsible for the upflowing air. Newton (1963) describes how dynamic forcing can be generated through wind shear acting on a severe convective storm. He suggests that as the advancing side of the storm moves faster than the low level air, a high pressure region forms near the cloud base; while upper-level environmental air moving faster than the storm generates a low pressure area in the lee of the cloud top. This creates an upward directed non-hydrostatic pressure gradient force on the advancing side of the cloud. The opposite pressure gradient force would form on the retreating side of the cloud. Newton proposes that these vertical pressure gradient forces accelerate parcels upward on the advancing side and downward on the retreating

side of the storm.

The updraft parcels, originating from near the surface, will tend to conserve their horizontal momentum, and as they rise will move more slowly than the surrounding air in a sheared environment. Relative to the environment, these updraft parcels have an upwind-directed motion. This results in an upshear tilt of the updraft, recently verified by in-cloud observations (Browning et al., 1976). Figures 1 and 2 show examples of the low level inflow and updraft. The negative slope of the updraft is an important feature in the strengthening of the severe convective storm by keeping the raindrops from falling through and creating a drag on the updraft. In this way, the sloping updraft of the severe storm will not destroy itself as occurs in non-severe storms having nearly vertical updrafts.

Browning and Ludlam (1962) have shown that hail will not attain a large size the first time through the updraft. If the updraft has an upshear slope in the lower half of the cloud, hail thrown forward from the top of the updraft can be captured by the strong low level inflow and carried back into the moist core. If the updraft is moist and buoyant enough, this second trip will form large hailstones. Therefore, an upshear sloping updraft is necessary for the formation of large hail-stones.

Downdrafts

Early investigators noticed that the decrease in air temperature after a heavy rain shower could not simply be explained by evaporation of raindrops into surface air. Equivalent potential temperature (θ_e) can be defined (Hess, 1959)

$$\theta_e = \theta \exp\left(\frac{Lr}{C_p T}\right) \qquad (1)$$

Here θ is the potential temperature, L is the latent heat of vaporization, r is the mixing ratio at the condensation point, Cp is the specific heat at constant pressure, and T is the parcel temperature at the condensation point. Because θ_e is conserved in both wet and dry adiabatic motions, Barnes (1946) and Browning and Ludlam (1962) have used this tracer variable to show the cold post-shower air as originating from middle tropospheric levels.

As suggested by Normand (1946) and later confirmed by Browning and Ludlam (1962), dry middle level air overtaking and flowing into the severe storm is accelerated downward by a drag force generated by rain falling out of the sloping updraft, and by rapid evaporation of the falling rain cooling the middle level air making it negatively buoyant. This downward accelerated air is known as the downdraft. Investigation has shown the downdraft vertical velocity and diameter to approximate that of the updraft. If enough rain is available this downdraft

will descend to the surface wet adiabatically and arrive with a temperature colder than the environment. The downdraft air tends to conserve its higher horizontal momentum and consequently has a downwind slope toward the advancing side of the storm (see Figure 2). Where the cold, high-momentum downdraft first meets the inflowing low level air, a mesoscale cold front occurs. This cold front, known as a gust front, acts like a wedge to the inflowing warm surface air and will help lift the air. The dynamics of this lifting process will be discussed in the next section.

Thus the sloping updraft helps create the sloping downdraft which helps maintain the updraft. It is this mutually advantageous structure which enables the severe convective storm to sustain an intense state for a long duration.

Energy

The origin of energy for the drafts in severe storm results from two sources: (1) conversion of horizontal kinetic energy to vertical kinetic energy of the inflowing air, and (2) forcing due to buoyancy (Ludlam, 1963). The downdraft-induced lifting of the inflowing surface air is a consequence of pressure perturbation gradients. The accumulation of cold dense air under the downdraft creates a perturbation high pressure area under it. Inflowing low level air approaching this high pressure area will be decelerated by the upwind horizontal

pressure gradient force, with a consequent reduction in the air parcel's horizontal kinetic energy. As the inflowing air loses horizontal momentum, it encounters a vertical non-hydrostatic pressure force and is accelerated upward. Thus the inflowing air is lifted and its vertical kinetic energy is increased.

The second source of storm energy, buoyancy, can be equated with changes in kinetic energy through integration of a form of the vertical equation of motion. For a scale analysis similar to that done by Holton (1973), the coriolis and curvature terms are small and can be neglected in the vertical equation of motion for a mesoscale convective system; resulting in

$$\frac{dw'}{dt} = -\frac{1}{\rho'}\frac{\partial p'}{\partial z} - g \qquad (2)$$

Here the primed letters refer to a parcel, w' is the vertical velocity of a parcel, p' is the pressure inside the parcel assumed to be the same as the environment at that height, ρ' is the parcel density, and g is the acceleration of gravity. By use of the hydrostatic equation ($\frac{\partial p}{\partial z} = -\rho g$) and the gas equation ($p = \rho R T_v$) where R is the specific gas constant for dry air, the buoyancy equation can be shown as

$$\frac{dw'}{dt} = g\frac{\Delta T_v}{T_v} \qquad (3)$$

Here T_v, the vertical temperature of the environment, is the same

variable as the gas equation, and is determined by

$$T_v = (1 + .61q)T$$

where T is the temperature and q is the specific humidity. The ΔT_v is the virtual temperature difference between the parcel and the environment, positive for the parcel warmer than its surroundings.

Equation (3) can be integrated with respect to height, and after use of the hydrostatic and gas equations, and suitable changes of variable, appears as

$$\Delta \frac{w^2}{2} = -R \int_{p_o}^{p} \Delta T_v \, d\ln p \qquad (4)$$

This shows that the change in vertical specific kinetic energy of the parcel is directly proportional to the difference between parcel and environment virtual temperature integrated over the pressure depth of a layer.

The mechanism maintaining the parcel temperature greater than the environment temperature is the latent heat release. Because these parcels originate from near the surface, this demonstrates the need for high moisture in the surface layers. This is confirmed in observational studies by Miller (1967) and Renne (1969) who conclude that surface dew points exceeding $12^{\circ}C$ are necessary for the occurrence of severe storms.

Equation (4) shows that the work needed to change the kinetic energy of a parcel may be calculated by measurement of the area between the environmental temperature curve and the lifted-parcel curve on a thermodynamic diagram. This is known as the parcel method. It assumes adiabatic motions and an environmental unaffected by these vertical motions. Although this method is simple to apply, investigation has shown that with the exception of the most energetic storms, cloud bases and tops predicted by the parcel method are higher than observed. This suggests changes are needed in the basic assumptions.

An improvement on the parcel method is the slice method as suggested by Bjerknes (see Beers, 1945). Using the principle of mass continuity, this method demonstrates that rising updraft parcels must be compensated by sinking environmental parcels; the upward flux of air must be balanced by a downward flux of air. The subsiding environmental parcels warm dry-adiabatically, thereby warming the environment. In this manner the heat surplus of the surface air is transported to higher atmospheric levels. As the number and intensity of storms increase in a region, the updraft area and correspondingly the rate of subsidence will increase. An increase in environmental stability results from this middle-to-upper level warming with a consequent reduction in parcel energy. Although the slice method gives a more realistic picture of convection, like the parcel method, it also

assumes adiabatic motions.

Stommel (1947) hypothesized that rising cloud parcels do not rise adiabatically. He suggested that as the cloud rises, environmental air mixes with the cloud parcel. Since the environmental air is cooler and drier than the parcel, the buoyancy of the parcel will be reduced as it mixes colder air and evaporates water to bring the mixed parcel back to equilibrium. This flux of environmental air into the cloud is called entrainment. As the radius of the updraft increases, the surface-to-volume ratio decreases; consequently decreasing the entrainment per unit volume with increasing size of the storm. Stommel (1947) estimated an entrainment rate of 200% for trade-wind cumulus; calculations by Byers and Braham (1949) exhibited entrainment rates of 100% per 500 mb for thunderstorms. Even this latter entrainment rate could still have a substantial damping effect on rising parcels.

A more accurate measure of the energy available to lift parcels could be made by reduction of the environment lapse rate by an amount equal to the subsidence warning, and increasing the parcel lapse rate by an amount representative of the entrainment. The new area on the thermodynamic diagram would be considerably smaller than with the parcel method. Unfortunately, these alterations in the lapse rates have complications which are not easily determined. Braham (1952) illustrates how downdrafts reduce the need for compensating subsidence

of the environmental air, and Palman and Newton (1969) discuss the variation of entrainment rates with location in the updraft. That is, parcels in the core of the updrafts are thought to arrive undiluted at their equilibrium level, but parcels in the outer sheaths of the updrafts experience strong mixing. Thus, although the parcel method has been found to have some defects, it is still the most used method for the measurement of energy available for convection.

The Making and Breaking of Inversions

Thus far the discussion has focused on three important conditions necessary for the occurrence of a severe convective storm: (1) High surface moisture, (2) dry air aloft, and (3) strong vertical wind shear. The two most important remaining requirements are (4) the low level inversion, and (5) the mechanism to locally destroy the inversion.

Investigations of conditions preceding severe weather outbreaks have shown the existence of a low level inversion which acts to inhibit convection (Fawbush et al., 1951; Mahrt, 1977). Without this inversion, convection on the scale of small cumulus clouds would rapidly mix the surface moisture with the middle level dry air, thereby preventing the buildup of low level moisture. The inversion may have several causes. During the spring and summer months, mixed layer induced inversions are formed almost everyday in the Plains states.

These inversions can also be substantially modified by subsidence and advections. Carlson and Ludlam (1968) suggest a source of the inversion as advection of potentially warm air from high plateau regions in Mexico.

The Great Plains states exhibit high surface moisture, dry air aloft, wind shear, and a subsidence type inversion frequently during the late spring and summer months, but at any particular location, severe weather outbreaks are still rare. This is because some kind of lifting mechanism is required to eliminate the inversion and allow deep convection. It is equally important that the inversion be overcome locally so that the moisture is not lost to numerous small cumulus clouds. The disappearance of the inversion near the time of severe weather outbreaks can be seen in tornado proximity soundings shown by Beebe (1958).

The elimination of the inversion occurs through a decrease in stability of the layer. The stability (s) of a layer may be defined (Fleagle and Businger, 1963) as

$$s = \frac{\partial \ln\theta}{\partial z} \doteq \frac{\Delta \ln\theta}{\Delta z} \qquad (5)$$

where θ is the potential temperature. Dry-adiabatic lifting of a layer results in a decrease of the layer stability because $\Delta \ln\theta$ remains constant, while Δz increases through the expansion of the layer with decreasing pressure. A similar analysis can be shown if the layer is

saturated. A significant destabilization can occur within a potentially unstable layer when lifting brings only the lower part of the layer to saturation, releasing the latent heat, thus differentially heating the layer. Often though, the greatest influence on layer destabilization is related to horizontal convergence. In this case, the increase of mass in the layer can lead to vertical stretching and a corresponding reduction in stability. Lifting and convergence working together can be very effective processes in the elimination of inversions.

Regions of lifting may be found where the air flow encounters solid obstacles, and above areas of low level convergence as shown by the equation of continuity (Holton, 1973)

$$\frac{\partial \omega}{\partial p} = -\left(\frac{\partial u}{\partial x} + \frac{\partial v}{\partial y}\right) \qquad (6)$$

Here ω is the vertical velocity in pressure coordinator $(\frac{dp}{dt})$, and u and v are the horizontal wind velocities on a pressure surface. Application of the Dines compensation principle (Petterssen, 1956) suggests that regions of strong low level convergence will be found directly under regions of upper level divergence. Thus lifting should be expected below upper tropospheric divergent regions. But the horizontal divergence in the upper troposphere is usually associated with positive vorticity advection (PVA) through the vorticity equation. Since upper tropospheric winds usually move faster than the disturbances, the local term in the simplified vorticity equation is small compared with

the advection term, leaving the vorticity equation (Palmen and Newton, 1969)

$$-\tilde{V} \cdot \tilde{\nabla}_p (\zeta + f) \doteq (\zeta + f) \tilde{\nabla}_p \cdot \tilde{V} \qquad (7)$$

Here $\tilde{V}$ is the horizontal wind velocity, ζ is the relative vorticity and f is the coriolis parameter. Thus with positive vorticity advection

$$(-\tilde{V} \cdot \tilde{\nabla}_p (\zeta + f) > 0)$$

there will be horizontal divergence ($\tilde{\nabla}_p \cdot \tilde{V} > 0$). Areas of strong positive vorticity advection can be found on the downwind side of troughs. PVA can also be found in the vicinity of the polar and subtropical jets. Beebe and Bates (1955) describe how divergence produced by the middle tropospheric jet maxima contributes to the elimination of the low level inversion. In their model, PVA produces divergence in the left front and right rear quadrants along the jet axis centered about the jet maximum. Recently, Whitney (1977) has illustrated the effect of the subtropical jet stream on severe thunderstorms. He shows the storms to be in the region where the polar jet and the subtropical jet are in a diffluent pattern. Thus, potential severe weather regions, due to lifting and vertical stretching should be expected in the vicinity of mountains, jet streams, and upper level troughs.

Stability may be decreased by other than vertical motions. Differential temperature advections can destroy an inversion as easily

as build one. Diurnal heating is ordinarily not strong enough to break the capping inversion itself, but its importance should not be overlooked in the total decrease of stability. It is usually the combination of diurnal heating and an appropriate mechanism such as vertical stretching which is responsible for the final release of instability.

III. SITE AND DATE DESCRIPTION

The southwest corner of the National Hail Research Experiment (NHRE) site lies 80 km NE of Denver, Colorado. The boundary of the operational area encompasses parts of three states; Colorado, Nebraska and Wyoming. This location was chosen because it lies within the region of maximum hail occurrence in the United States. Figure 3 shows the five rawinsonde station locations within the network; included are station elevations and mean summertime mixing ratios.

The climate of this region has most of the elements common to the interior of large continents in middle latitudes: low humidity, light rainfall, hot summers, cold winters, and large variations in temperature and rainfall from year to year. The mean annual rainfall is 38 cm (15 inches) with approximately 70% of this occuring during the growing season from April to September. The maximum daily temperature in mid-summer can exceed 40°C, with the mean maximum temperature in June and July about 30°C (U.S. Weather Bureau, 1964).

The Rocky Mountains, 80 km to the west, have a strong influence on the climate of the region. The great height of these mountains (> 4000 m) causes sufficient drying of the air carried from the Pacific Ocean so that the only significant source of moisture is the Gulf of Mexico. As a result of the long trajectory over the Gulf, the

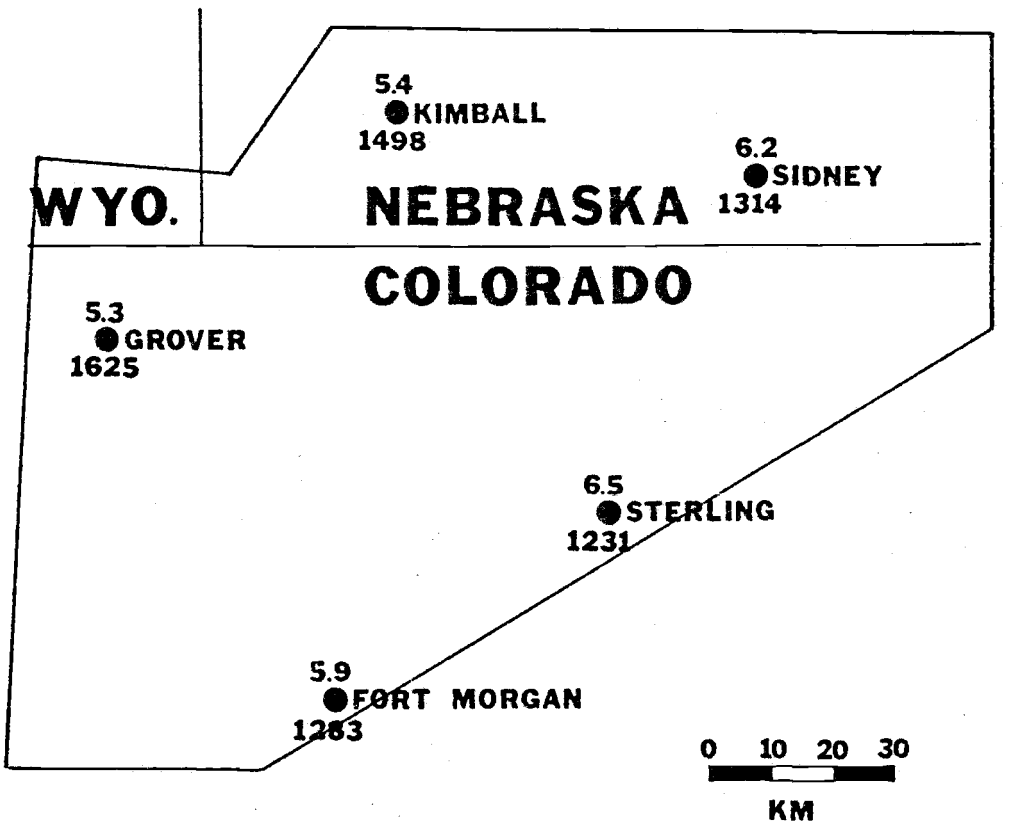

Figure 3. NHRE network for 1973-74, including the five upper air stations used in the experiment. Shown are average summertime (15 May-10 Aug.) 1220 MST mixing ratios (g/kg) in the lowest 100mb, 1972-74. Station elevations are in meters. Add seven hours to convert MST to Z time. From Mahrt (1976).

anticyclonic winds of the Atlantic High carry moist air inland to the Great Plains during the spring and summer months. Higher than average moisture values occur with the migration of a surface low-pressure region to the east of the Rocky Mountains. This will strengthen the pressure gradient and induce a strong southeasterly flow of warm moist air.

Radiosondes were released at three hour intervals, 0920, 1220, and 1520 (MST), every day during the spring and summer months at the five network rawinsonde stations. Unfortunately the release times do not correspond with the National Weather Service radiosonde release times, 0500 and 1700 (MST), nor with the 3-hourly surface observations, 0200, 0500, 0800, ... (MST). Additional surrounding synopic radiosonde data were obtained from the Northern Hemisphere Data Tabulations from the Environmental Data Service (1973), Asheville, North Carolina.

NHRE hourly surface reports were used from Grover and Sterling, with Sidney and the surrounding area surface reports obtained from the Environmental Data Service.

The satellite photos were taken by NOAA 2 and display images taken near 09L (local time) and near 21L.

IV. THERMODYNAMIC VARIABLES

Hourly surface reports for the Great Plains region for 27 June 1973, (the first day), show small cumulus through the afternoon with scattered thunderstorms during the late evening. Within the NHRE network, the same conditions prevailed, with a non-severe thunderstorm beginning at 2100 MST at Sidney. On 28 June 1973, (the second day), widespread thunderstorm activity occurred over Colorado, Kansas, New Mexico, Oklahoma and Texas. The NHRE network experienced severe thunderstorms (hail larger than 3/4 inch) and even an unverified funnel cloud in the late afternoon that day.

Mahrt (1977) has statistically found a linear combination of variables which discriminates between hail days and non-hail days. He finds that high values of low level moisture, a shallow mixed layer, significant low level stability, and weak stability above the LCL (lifting condensation level) are indicative of hail days.

The vertical structure within the NHRE network at 1520 MST is indicated by composite profiles of potential temperature and mixing ratio (Figure 4) for 27 and 28 June 1973. These composite profiles were made by averaging the respective variables at 25 mb intervals for the five stations within the network. For the two days, the average depths of the mixed layer, a layer of $\frac{\Delta\theta}{\Delta p} \doteq 0$, is shown by the respective thicknesses from surface to letters A and B. The hail

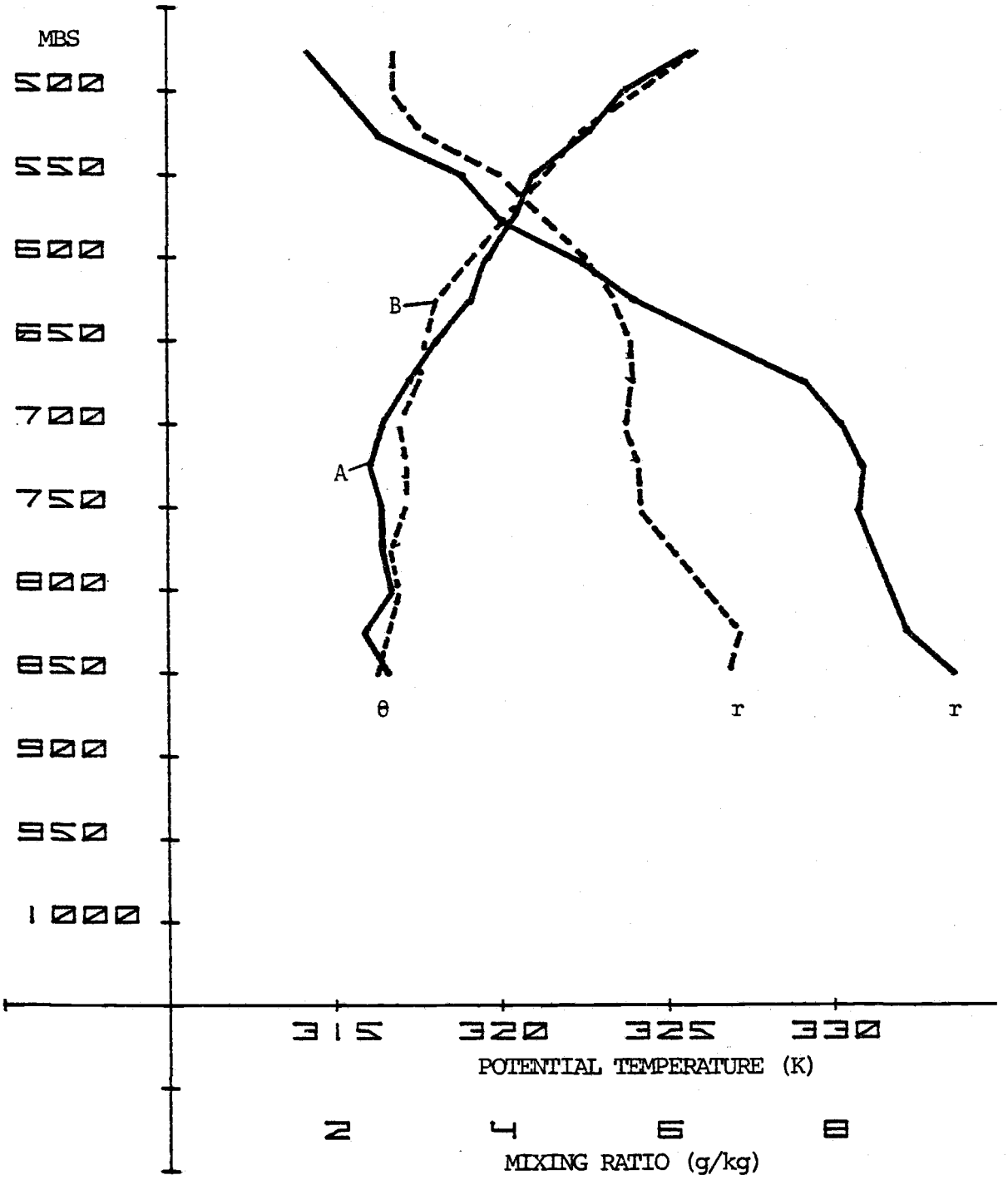

Figure 4. Composite profiles of potential temperature θ (left) and mixing ratio r (right) for NHRE network at 1520 MST. Dashed lines are for 27 June 1973 and solid lines are for 28 June 1973. The letters A and B indicate the tops of the respective mixed layers.

day and non-hail day are distinguishable by two features in this figure: (1) The hail day has a shallower mixed layer depth, and (2) the hail day has a greater mixing ratio (2g kg^{-1} larger) in the mixed layer. The slightly warmer low level potential temperature profile on 27 June is probably not significant, as statistically suggested by Mahrt (1977). Isentropic vertical cross sections at 00Z for both days (not shown) also show the second day to have a shallower mixed layer depth.

Hourly surface reports within the NHRE network show 27 June 1973 to be slightly warmer than 28 June 1973 throughout the day. A three station average of the maximum temperature shows 27 June at 31.0°C and 28 June at 29.7°C. Neither of these surface temperatures significantly differs from the June-July climatic maximum temperature of 30°C (U.S. Weather Bureau, 1964). Dew points on 27 June range from 7° to 9°C throughout the day, increasing to 15°C in the late evening after rain showers began. The 28th had consistently higher dew points of 13° to 15°C throughout the day. Surface winds were light both days except at the time of thunderstorms. Thus the only significant difference in surface conditions between the two days was moisture.

An analysis of the mean mixing ratio for the mixed layer, taken to be 150 mb deep (Figure 5a and 5b), shows the two days to have quite different patterns. At 00Z 28 June, a very large region of moisture is located to the far southeast of the NHRE network. This

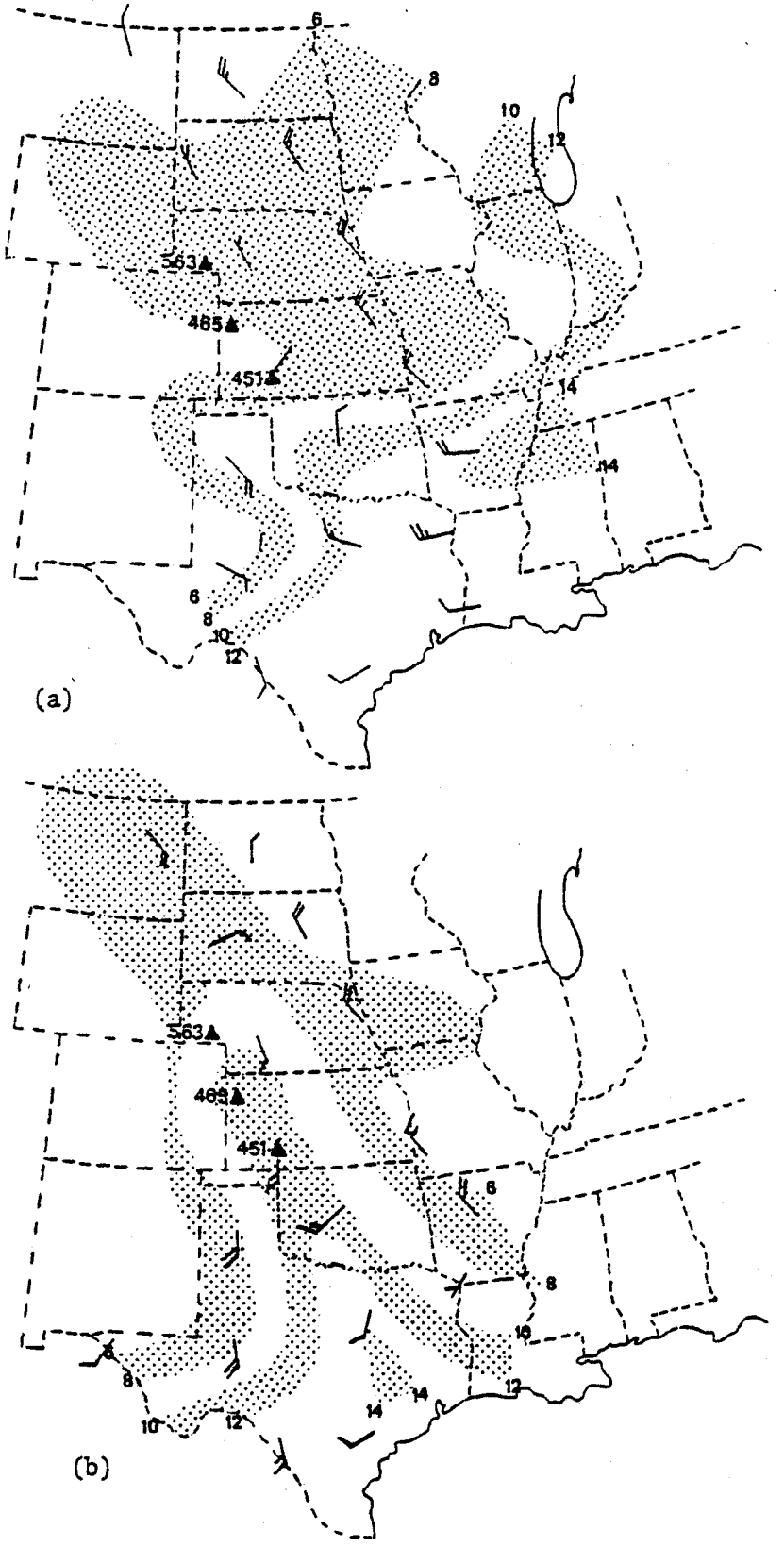

Figure 5. Mean mixing ratios in the lowest 150mb in g/kg, for (a) 00Z 28 June 1973, and (b) 00Z 29 June 1973. Darkened triangles are station locations discussed in the text. Winds are at 850mb.

pool of moisture and the gradient of moisture to its north and west are principally due to the northwesterly flow of cold dry air associated with the cold front extending from the Great Lakes to western Texas. These northwesterly winds act against the advection of any moisture from the southeast United States into the Great Plains. Northeastern Colorado lies in an area of small moisture gradient with mean 150 mb deep mixing ratios of 6.2 g kg^{-1}, which is near the mean summertime moisture values found by Mahrt (1976) for the NHRE network (see Figure 3).

By 00Z 29 June, the frontal zone has weakened and moved farther to the east, allowing a moist southeasterly flow to penetrate into the Great Plains. The associated mixing ratio ridge at this time, is a classic example of the moisture ridge described by Fawbush et al. (1951) as an indicator of severe weather. Any outbreaks would be expected to occur in the northwest region of this ridge. Mean mixing ratios in the lowest 150 mb within the network were between 9 g kg^{-1} and 10 g kg^{-1} at this time, which are considerably higher than mean summertime values (Mahrt, 1976).

The increased moisture from 27 June to 28 June can be realized by several means: (1) The previously discussed shallower mixed layer on 28 June will have a higher moisture content due to weakened downward entrainment of dry free-flow air into the mixed layer, (2) there could be moisture flux convergence into the region between

the two days, and (3) evapotranspiration could be important.

The NHRE network is situated in the western foothills of the Rocky Mountains where natural vegetation is characterized by grasslands and sagebrush. Estimation of evapotranspiration is difficult without specific measurements; none were taken by NHRE. Therefore, the only possible method of estimation is the empirically derived Thornthwaite method (see Palmer and Havens, 1958). According to Penman (1948), "The method itself is not based on sound theoretical meteorological principles, but it gets surprisingly good results." By using the maximum and minimum temperatures of the day, the potential evapotranspiration was computed using the Thornthwaite method. The potential evapotranspiration is the evaporation which would take place if the ground were water-saturated. To convert to actual evapotranspiration, a determination of the soil moisture content must be made; this was not available. A U. S. Department of Commerce report (Wyoming State Climatologist, est. 1964) for Wyoming showed potential evaporation and actual evaporation (evapotranspiration) values for stations within 80 km of the network and having the same general topographical and irrigation features. A simple proportionality was then used to estimate the actual evapotranspiration for the network stations on 28 June 1973. After mixing the evaporation through a mixed layer of 150 mb, mixing ratio increases of 1.0 to 1.5 g kg^{-1} were computed, which compared favorably with observed mixing ratio increases that

day. Since daily weather records indicate similar soil conditions, wind, and air temperatures for both days, comparable evaporation rates would be expected. As the dew point was not reached during the intervening night, the evapotranspiration for the two days would be somewhat cumulative, accounting for a part of the increased moisture on the second day.

The 850 mb winds plotted on Figure 5a and 5b show a strengthening of the southeasterly flow by 00Z 29 June. The change in surface winds at stations along the axis of the 00Z 29 June moisture ridge is shown in Table 1.

Table 1. Surface winds in degrees for three Great Plains stations. Dates indicated are for June 1973.

Station	12Z 27 June	00Z 28 June	12Z 28 June	00Z 29 June
Sidney 563	290°	260°	170°	80°
Goodland 465	310°	120°	150°	150°
Dodge City 451	20°	320°	250°	180°

The three selected stations are indicated on Figure 5a and 5b by darkened triangles. Surface winds on 27 June show a backing with time with a westerly component through most of the day. By 28 June the wind has backed to the south with some easterly component. This 180° change in wind direction is due to a reversal of the surface

pressure gradient. Surface analyses (not shown) reveal northeast Colorado in a high pressure region on the first day, and in a low pressure region on the second day. The large pool of moisture, shown on Figure 5a, will be advected northward by these southeast surface winds on 28 June.

Calculations of the low level moisture flux into the NHRE network on 28 June show potential mixing ratio increases on the order of 1 g kg^{-1} per three hours in the mixed layer (150 mb deep).

Moisture flux convergence appears to be the primary source for the increase of low-level mixing ratio over the two day period. The shallower mixed layer depth on the second day contributed to the maintenance of the high moisture values by entraining a lesser volume of dry upper-level air into the mixed-layer. Although difficult to quantify, evapotranspiration seems to be significant to the total water vapor budget and should not be neglected.

High surface temperature and moisture are necessary ingredients for severe storm initiation. A useful variable in severe weather analysis is equivalent potential temperature (θ_e), because it combines the latent and sensible heats into one variable. Anderson and Uccellini (1973), in a study of thunderstorms in the NHRE area, have shown that "The axis of maximum θ_e favorably correlates with the area of initial cell development for both air mass and frontal cases."

Surface θ_e was calculated for the two days in the Colorado region

using temperature, dew point, altimeter setting, and station elevation as input (Figure 6). At 12Z 27 June, a tongue of high θ_e extended up through the Rocky Mountains with an easterly branch into Nebraska. By 00Z 28 June, the θ_e ridge has shifted eastward and is now considerably east of the mountains. The earlier maximum at Sidney, Nebraska is still evident.

On the morning of 28 June 1973 (12Z 28) the ridge intensifies east of the mountains, and has a definable gradient to both the east and the west. Again the high mixing ratio to the northeast of Colorado gives Nebraska high values of θ_e. The late morning and afternoon maps show the θ_e ridge to continue to move slowly eastward through the day.

Within the NHRE network, θ_e is higher through the day on 28 June than on 27 June. The values at 00Z 29 June might have been higher except that severe storms were occurring at this time and the downdrafts were bringing down middle-level air of low θ_e. The stippled area on the maps indicates the location of the NHRE network. Notice that at 00Z 29 June, the network lies at the northwest tip of the θ_e ridge, a most favorable area for severe storm initiation. The X on this map marks the site where the 2 cm hailstones fell.

Besides its usefulness in surface analysis, θ_e can also be a convenient indicator of atmospheric potential instability when plotted in the vertical. Potential instability is an important property of a

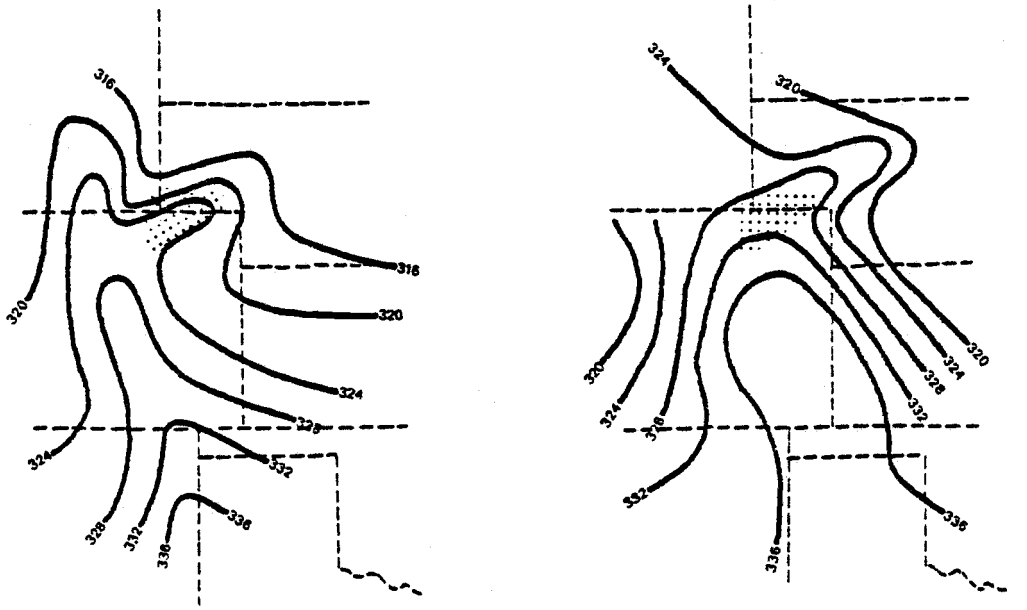

Figure 6. Surface θ_e (K) analyses at indicated times for June 1973. The NHRE network is shown as the stippled area; the X marks the site of the 2cm diameter hail fall.

layer, because if some lifting mechanism were present, such as a front or an upper level short wave trough, static instability could be ahieved within that layer. As discussed by Rossby (1932), the criterion of $\partial\theta_e/\partial z < 0$ within a layer is a necessary and sufficient condition for potential instability. Figure 7 displays vertical profiles of θ_e for Sidney at 1520 MST for both days. The 27 June profile displays a potentially stable layer from surface to above 500 mb, whereas the 28 June profile shows θ_e decreasing with height, indicating potential instability. The two days exhibit a five degree celsius difference in θ_e temperatures in the lowest 150 mb, a result of the greater moisture on the second day.

The energy available for vertical motions within a layer may be calculated on a thermodynamic diagram by measurement of the area between the environmental temperature curve and the lifted-parcel curve, as shown by equation (4). If the energy decreases with height (negative area), the layer is statically stable. If the energy increases with height (positive area), the layer is statically unstable. Although the method is physically sound, in practice it is rarely used because the calculations are too time consuming. However, a good estimation of the energy change with height (the static stability) can be achieved by differencing the environment and parcel temperatures at just one predetermined level, and using this temperature difference as a static stability index. Barber (1973) found a correlation coefficient of .98

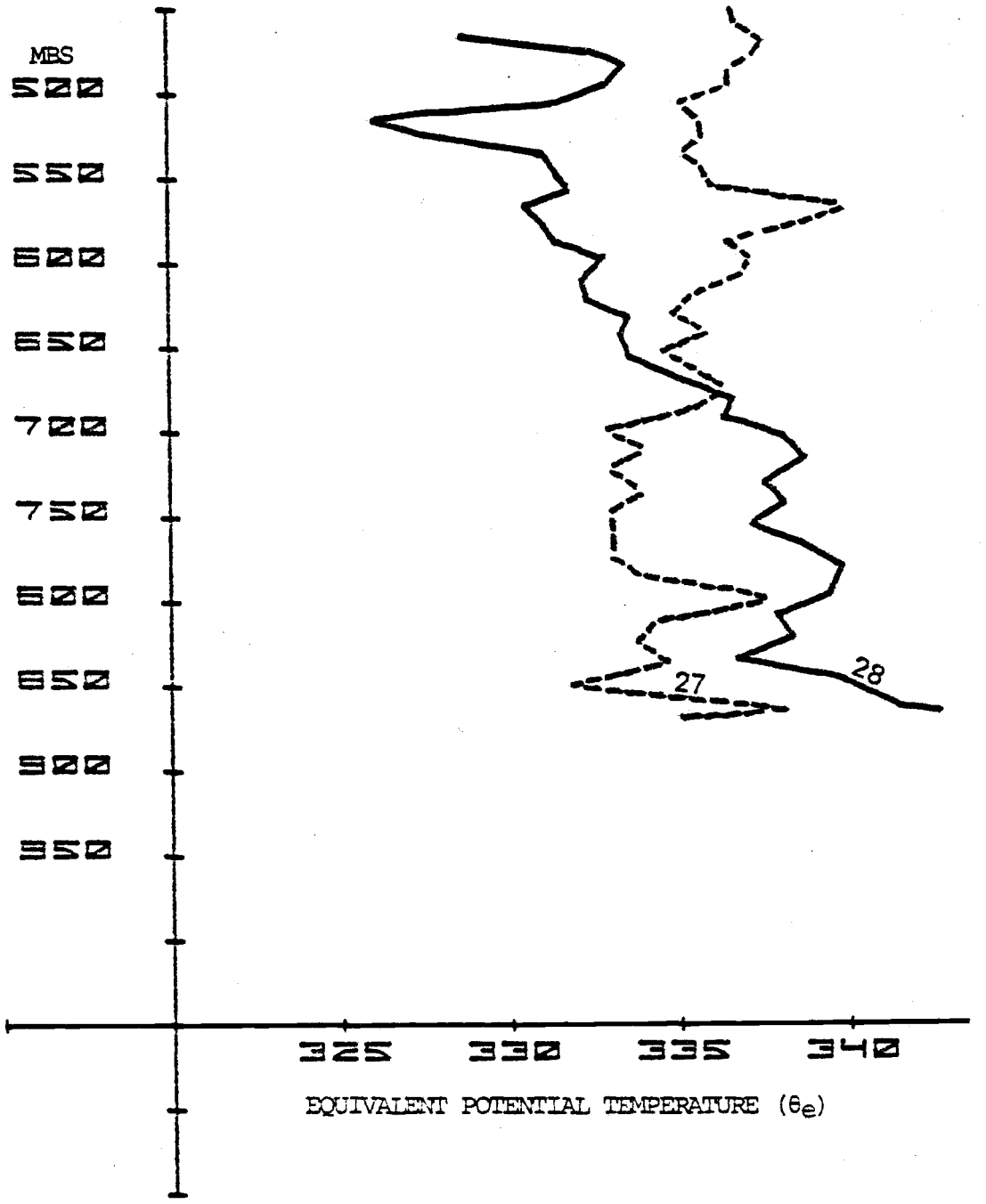

Figure 7. θ_e (K) profiles for Sidney at 1520 MST on 27 June 1973 (dashed line) and 28 June 1973 (solid line).

between energies computed from equation (4) and the lifted index. The lifted index is defined by Galway (1956) to be the difference between the parcel and environment temperatures at 500 mb for a parcel lifted adiabaticaly from the mixed layer. Negative values indicate instability.

Individual station static stabilities hereafter referred to as stabilities, were computed using a method similar to the lifted index. In this case, a parcel having properties of the lowest 100 mb is lifted adiabatically to 400 mb and its temperature subtracted from the environmental temperature at that same level. Here also the stability decreases with decreasing index values. Figure 8 shows the computed stability index values for 27 and 28 June 1973 at the five NHRE network stations plotted as a function of time. There is a noticeable scatter of stabilities at each time period, somewhat surprising for stations so near one another. Barnes (1974a) notes a similar scattering in plotted lifted index values from 49 soundings taken over the mesonetwork of the National Severe Storms Laboratory. He concludes that individual stabilities may not be representative of the surrounding area. The regression line shows the best linear fit for all the data. Both days show a steep decrease of stability through the day, mostly just due to diurnal surface heating. The important point brought out, though, is the high positive stability seen on the morning of 27 June in contrast with the low positive stability seen on the morning of 28 June. Given these starting values and the usual diurnal destabilization

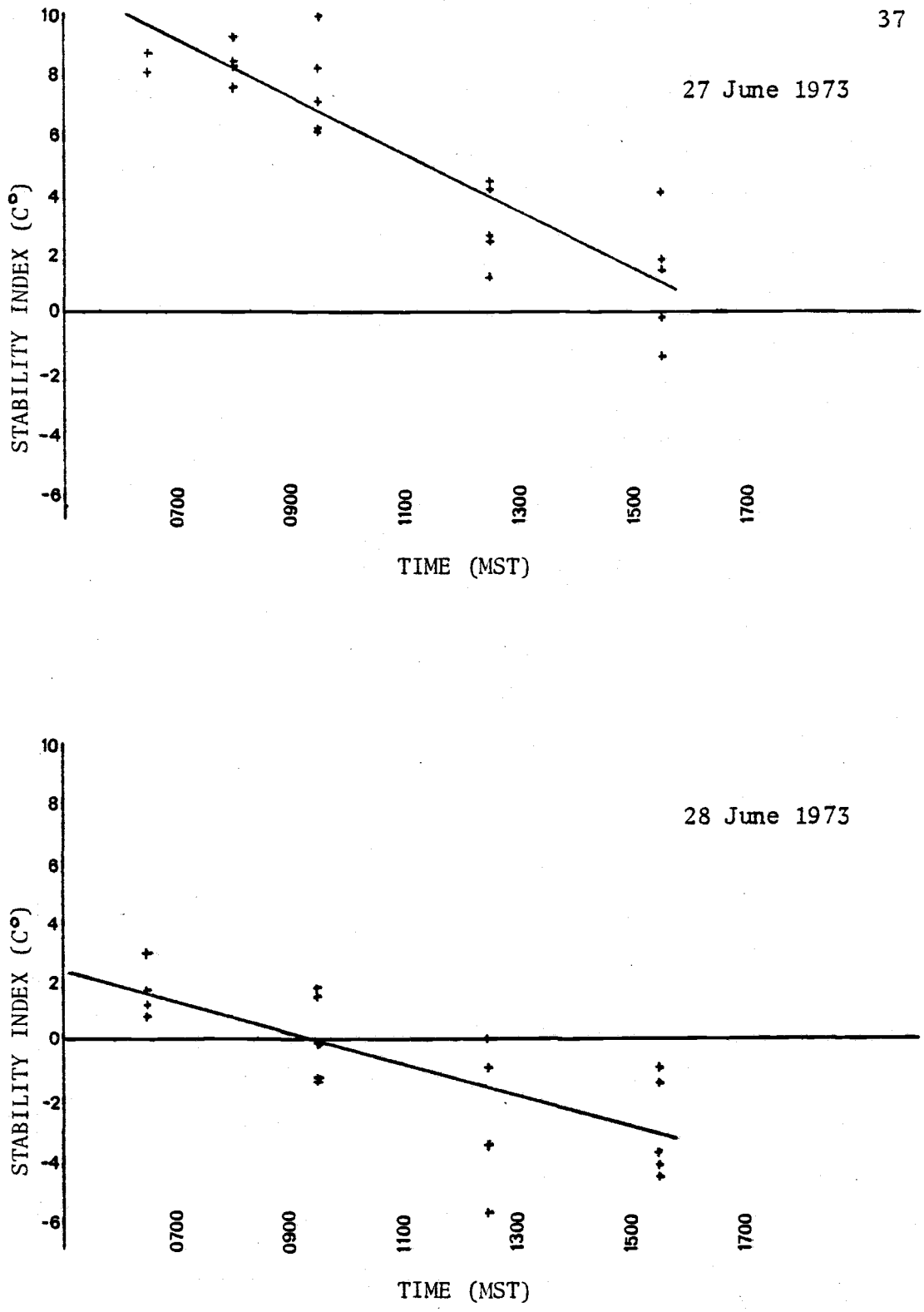

Figure 8. Lifted stability indexes vs time for five NHRE stations on 27 June 1973 (top), and 28 June 1973 (bottom). Diagonal line is regression line which shows the best fit of the data.

through the day, it should be no surprise that the second day had much stronger convective activity than did the first.

The lower stability on 28 June 1973 is principally due to the increased moisture in the low levels, and to a lesser degree to the colder 400 mb temperature that day. As we shall see later, rising motions and low level convergence also play a part in the destabilization on the 28th.

Thus far temperature, moisture, and stability for the two days have been discussed. Because a single observation of variables may not be representative of the surrounding area, the thermodynamic variables used in the determination of the lifted index were spacially averaged at each time period using the five NHRE network stations. These station-averaged variables were then used to compute a mean static stability index for the NHRE network at each time period. Table 2 shows five-station averages at selected times. θ_{100} is the mean potential temperature for the lowest 100 mb. r_{100} is the mean mixing ratio for the lowest 100 mb, T_{400} is the environmental temperature at 400 mb, and static stability index is the resultant lifted stability index using those same variables. The afternoon mean potential temperatures appear to be the same for both days. The mean mixing ratios increase through the first day and stay consistently high through the second. The temperature at 400 mb shows a systematic decrease through the two day period probably due to cold air advection and/or

ascent associated with the short wave trough. The mean stabilities again show the same results as the regression analysis of the individual station stabilities, with the morning stability lower on the 28th than the 27th, and decreasing stability through both days.

Table 2. Averaged variables for the five NHRE stations.

Time (MST)	θ_{100}(K)	r_{100} (g/kg)	T_{400} (^{o}C)	Static Stability Index(C^{o})
		27 June 1973		
0920	309.5	6.15	-16.8	+7.0
1220	315	7.0	-16.3	+2.8
1520	317	6.6	-17.9	+0.6
		28 June 1973		
0920	312	8.8	-18.4	-0.4
1220	315	8.8	-19.0	-2.2
1520	316.5	8.85	-18.9	-2.9

V. SYNOPTIC ANALYSIS

The dominant synoptic scale feature on 27 and 28 June 1973 was a mid-tropospheric and upper-trospheric ridge extending from Arizona to eastern Montana, resulting in northwesterly flow aloft over the NHRE network. Standard analysis of the 500 mb map for the mornings of both days show this ridge to have relatively smooth flow, i. e., an absence of short waves. Surface analysis shows the network is an area of weak high pressure with a distant frontal system located from the Great Lakes to Texas on 12Z 27 June, and even farther east by 12Z 28 June. The absence of any outstanding synoptic features normally associated with severe convective storms near the NHRE network on the morning of the 28th makes this severe weather outbreak atypical of the usual cyclone induced case.

The NHRE Meteorological Summary (Fankhauser et al., 1976) shows a computerized 500 mb analysis for 00Z 29 June (Figure 9). Although the height contour analysis shows only a weak trough over the network at this time, the temperature trough to the west suggests that significant vertical motions are associated with this trough. The remainder of this chapter will describe the various techniques employed to bring out the structure, intensity and track of this disturbance.

Careful hand analyses of the 700, 500 and 300 mb height and wind data from 12Z 27 June 1973 to 12Z 29 June 1973 reveal the

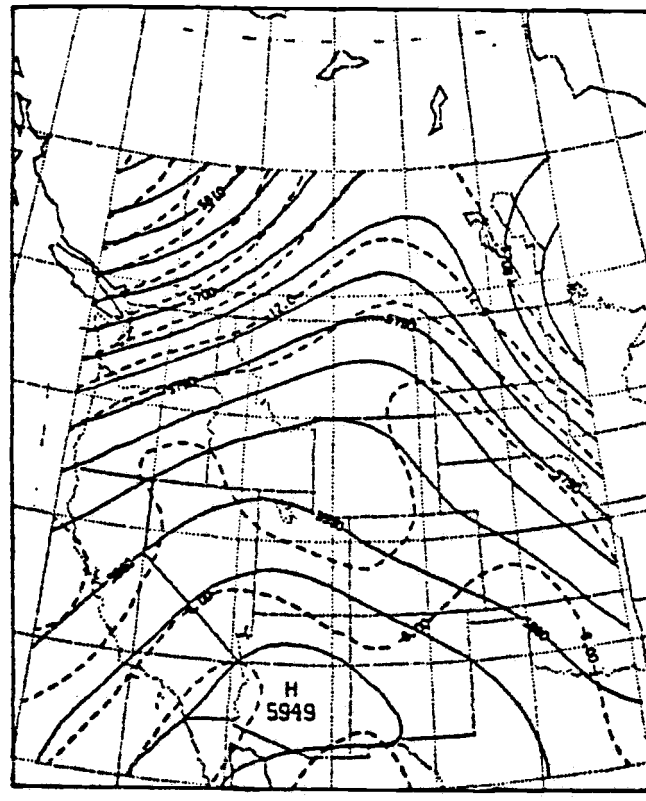

Figure 9. Computer drawn 500mb analysis for 00Z 29 June 1973. Solid lines are contours and dashed lines are isotherms. After Fankhauser et al., 1976.

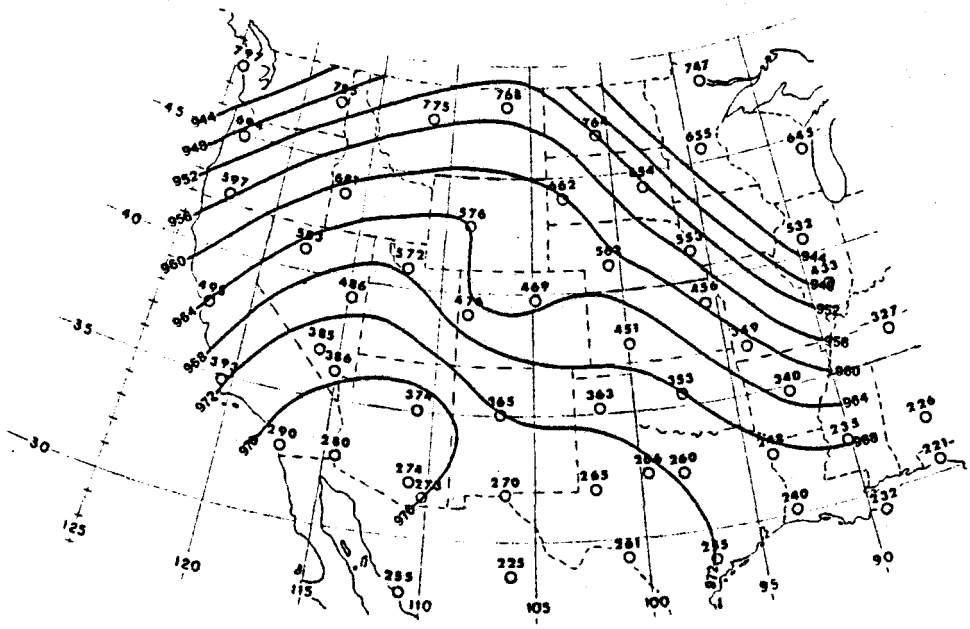

Figure 10. Hand drawn 300mb contour analysis for 00Z 29 June 1973.

movement of a weak short wave trough along the ridge contours. The trough first appears in the data at 00Z 28 June on the California coast. Following the large scale flow, it moves across Colorado on 28 June, and by 12Z 29 June the trough is found in the Texas-Oklahoma panhandle region. The clearest representations of the short wave trough were found at 300 mb; Figure 10 displays an example at 00Z 29 June. Although Figures 9 and 10 are for the same time, the trough at 300 mb (Figure 10) appears to be better defined than at 500 mb (Figure 9). This is principally a result of the upward intensification of the trough, a direct consequence of its cold core. Figure 9 is probably more smoothed than is the hand drawn analysis also.

As the trough propagated from the west coast to Oklahoma, the small scale of the trough and the wide spacing between upper air stations made continuity of positioning and structure difficult. Often the existence of the trough was detected from data from only one station. This problem led to a station time-continuity analysis.

A time-continuity verification was made by use of a time cross-section of 300 mb winds (Figure 11) along the track of the trough. Because the large scale ridge moved so slowly during the two day period studied, the assumption was made that the disturbance was superimposed on some steady state mean flow, and a shift in the wind at a station between time periods should indicate the trough approach

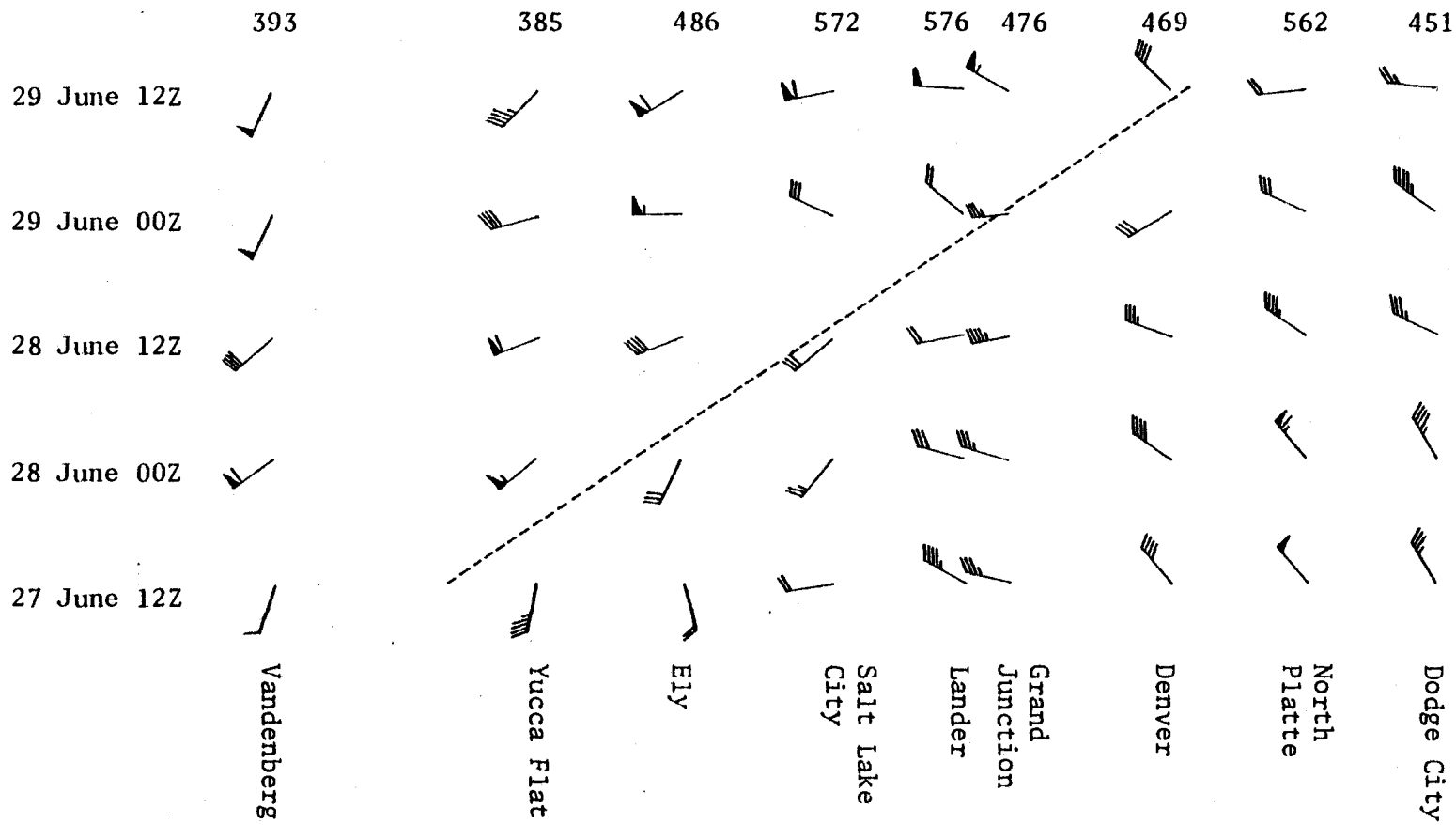

Figure 11. Time cross-section of 300mb winds along the track of the trough. The slope of the dashed line, which indicates the approximate location of the trough, suggests that the trough moves at about 25kts.

or passage. Beginning after 12Z 27 June, a veering of the wind can be seen progressing across the country from Yucca Flat, Nevada (Station 385), through Denver, Colorado (Station 469) shortly after 00Z 29 June indicating trough passage. The slope of the dashed line which indicates the approximate location of the trough suggests that the trough is moving at about 25 kts.

In the time cross-sections, a short wave passage was determined by wind direction deviations from a steady state mean wind. This suggests a more sophisticated depiction of the trough passage by dividing the observed wind into a time mean-part ($\bar{\tilde{V}}$) and a perturbation-part ($\tilde{V}'$). To obtain a mean wind, the flow should be averaged over a long enough interval of time to average out the short wave fluctuations yet still short enough to preserve the trends in the large-scale flow field. The winds from five time periods (12Z 27 June 1973 - 12Z 29 June 1973) at each station were averaged to get the mean wind, and then subtracted from the observed winds to get the perturbation winds. Streamlines of the mean winds display a smooth contour ridge over the western two-thirds of the country; and the perturbation winds, with the assistance of a time-to-space conversion (see Fujita, 1963), reveal a cyclonic vortex moving along the contour ridge (not shown). Although north and south perturbation winds were expected on the west and east sides of the trough, the unexpected west and east winds of the vortex are apparently due to

increased wind speeds to the south of the trough and decreased wind speeds north of the trough.

Since later calculations of divergence and vorticity could be simplified by the use of an evenly spaced grid network, all station data were processed by an objective analysis scheme. Using the Barnes Analysis (Barnes, 1973) as modified by D. A. Barber which obtains grid points through a weighting factor which exponentially decreases with distance, the 300 mb perturbation winds were analyzed for the four time periods from 00Z 28 June to 12Z 29 June (Figure 12). At 12Z 27 June, the perturbation vortex is off the California coast in an area of no data, and is not shown. At 00Z 28 June, the vortex is clearly seen in central California. By 12Z 28 June, a stronger and more organized circulation is seen over Utah. At 00Z 29 June, the perturbation vortex winds have intensified somewhat with the center now in western Colorado. At 12Z 29 June the vortex loses some of its organization and is centered over the Oklahoma Panhandle. The speed of movement of the perturbation vortex is approximately 20-25 kts, in good agreement with the preliminary estimate of 25 kts based on the time cross-section.

Figure 13 displays the perturbation winds on 00Z 29 June for 700, 500, 400 and 300 mb. As can be seen, the vortex is clearly visible only at 300 and 400 mb, with some cyclonic wind organization noticeable at 500 mb. At 700 mb only a shear zone south of the

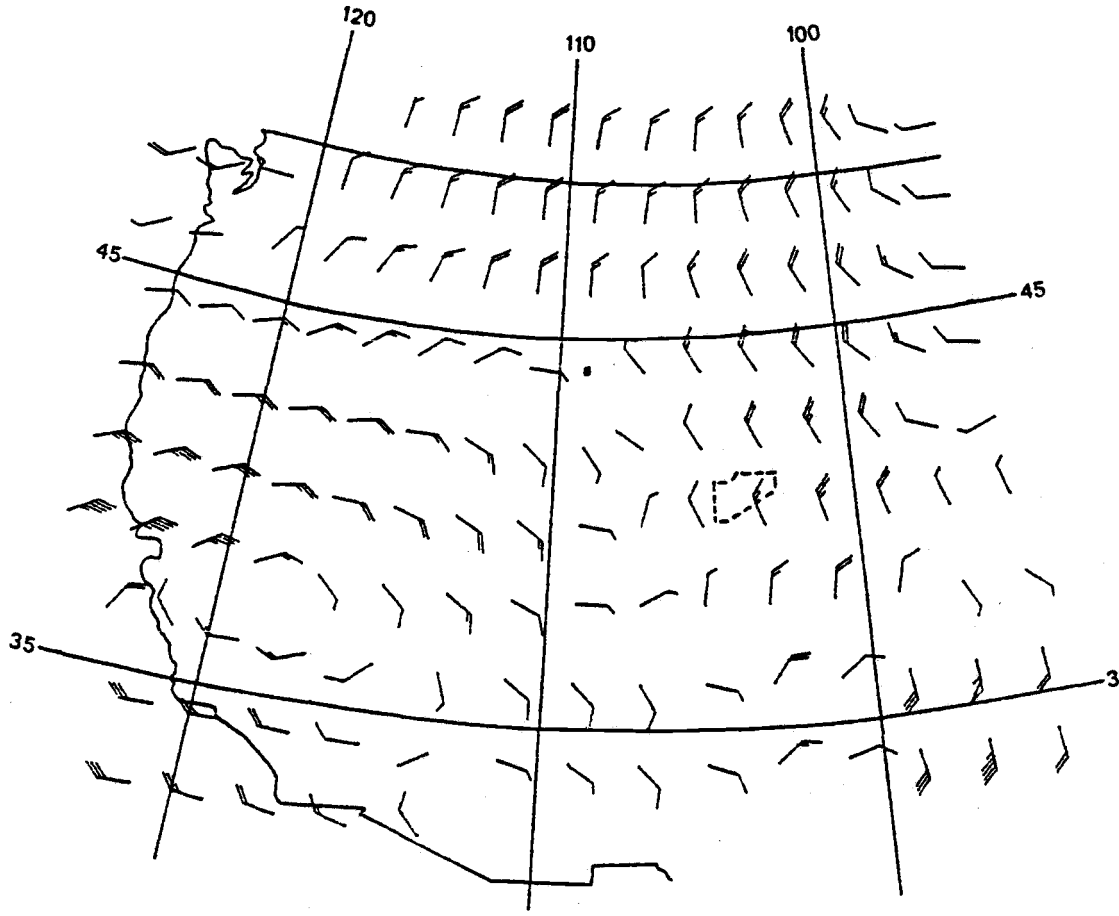

Figure 12. 300mb perturbation winds. Full barbs on wind arrows indicate 10kts, half barbs 5kts. Dashed area is the outline of the NHRE network. Notice the vortex centered about southern California. Figures 12b,c and d show the progression of this perturbation vortex across the U.S.

(a) 00Z 28 June 1973

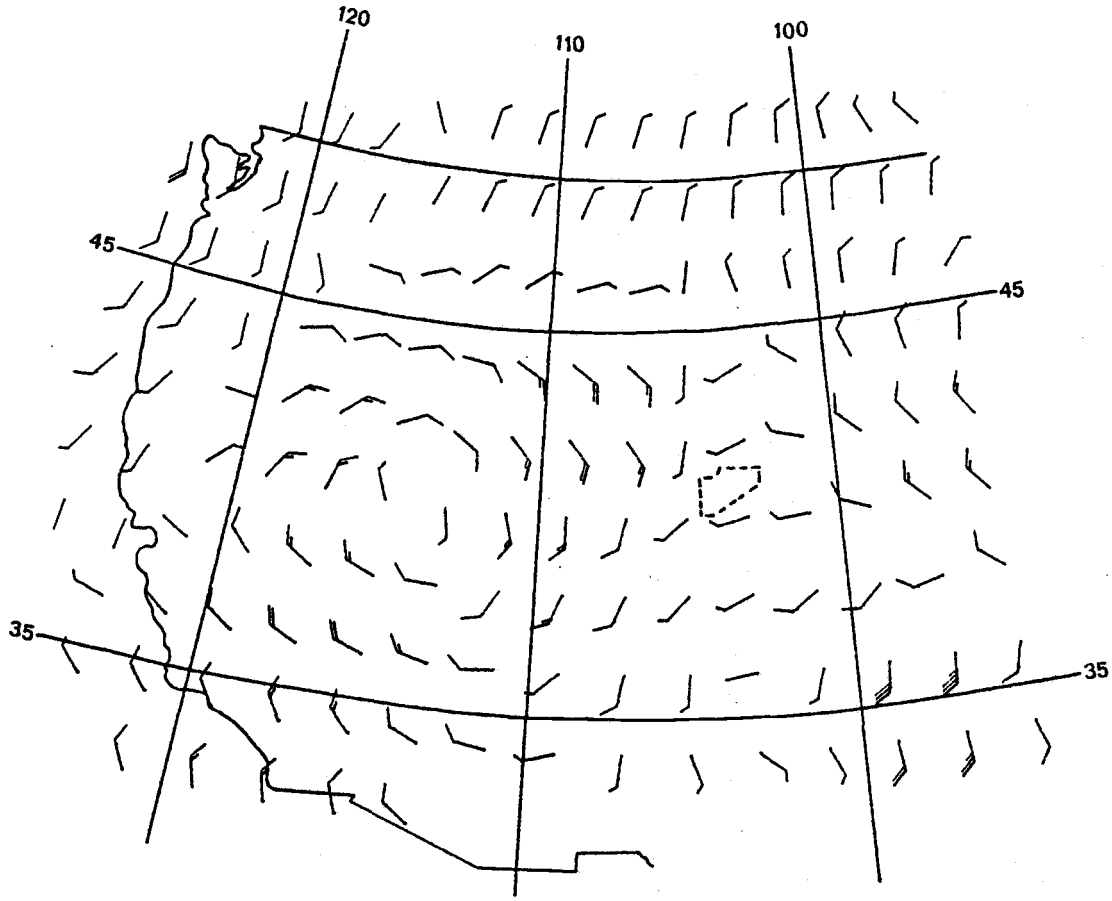

Figure 12 continued

(b) 12Z 28 June 1973

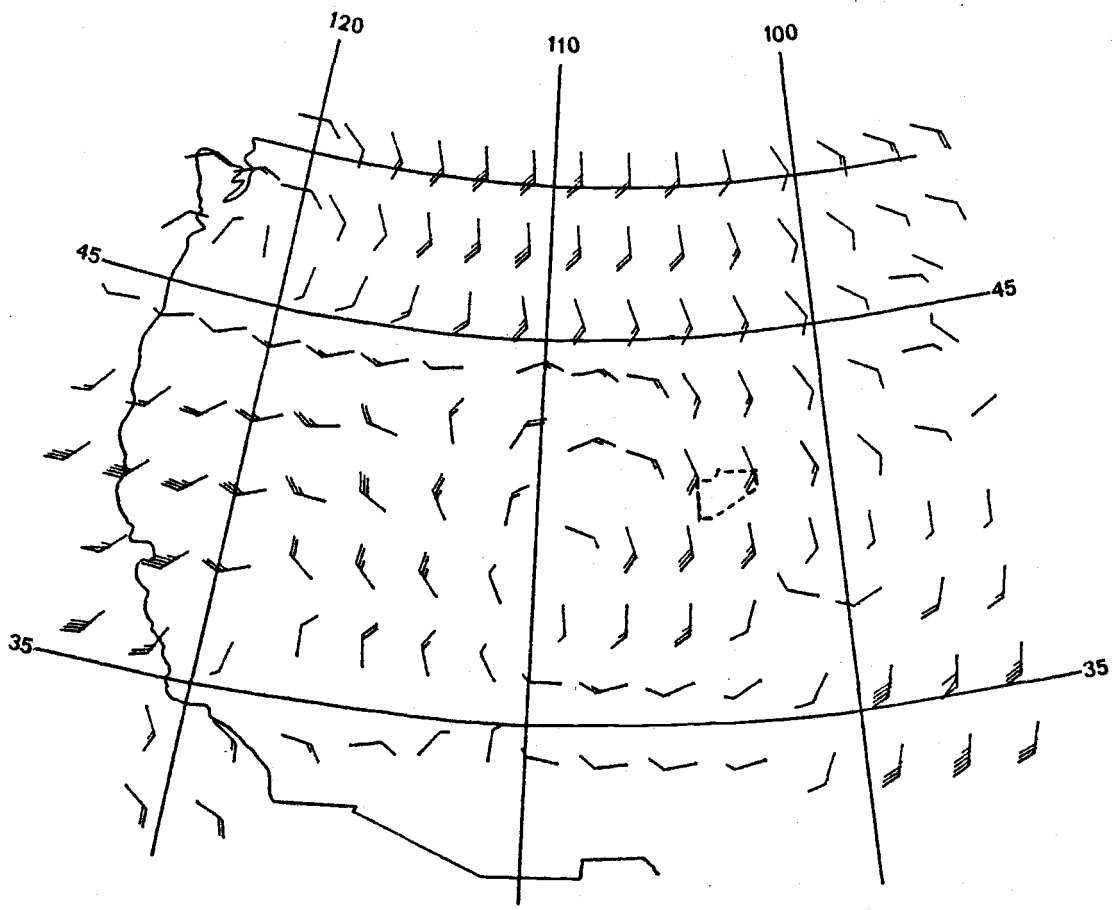

Figure 12 continued

(c) 00Z 29 June 1973

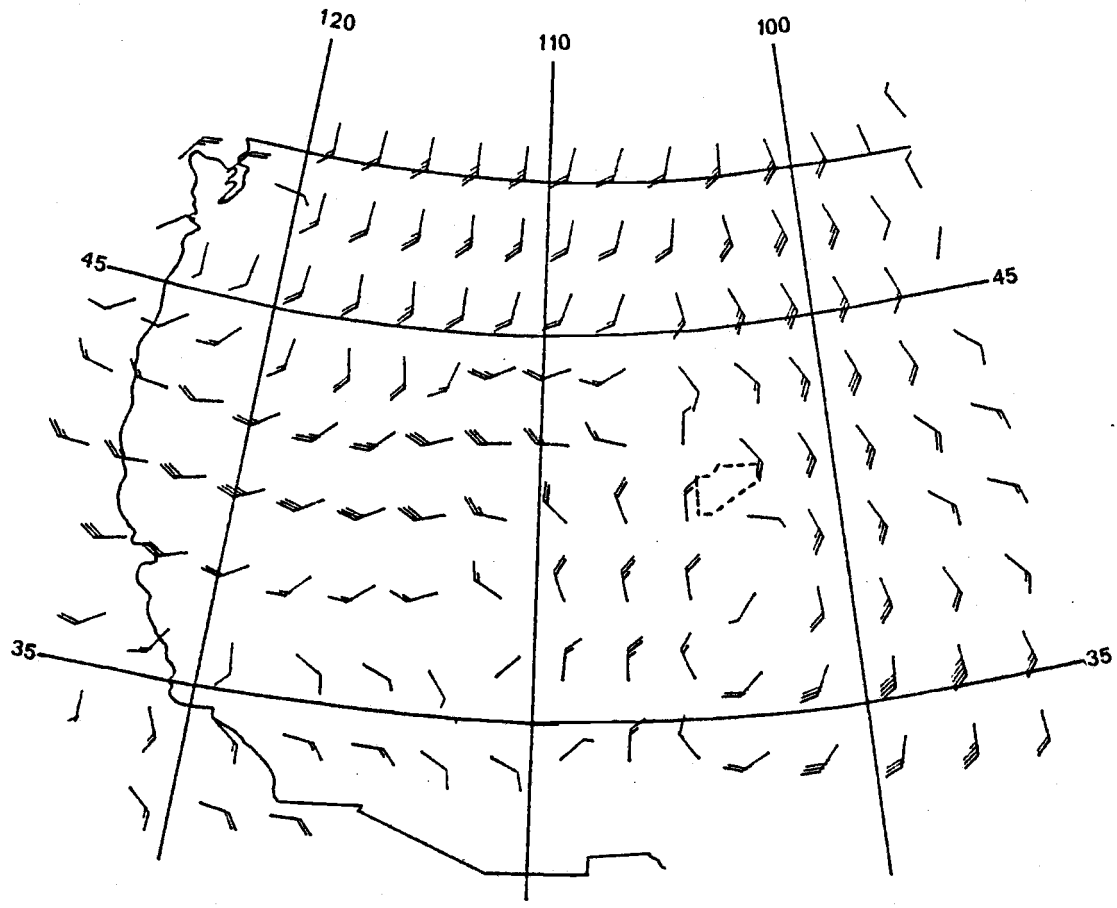

Figure 12 continued

(d) 12Z 29 June 1973

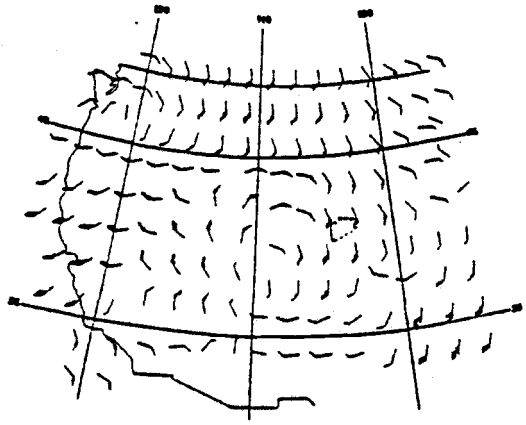

300mb

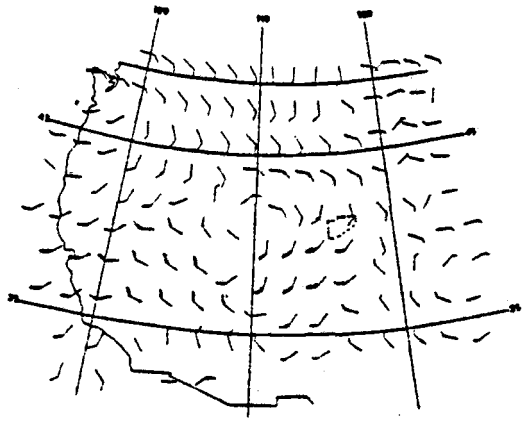

400mb

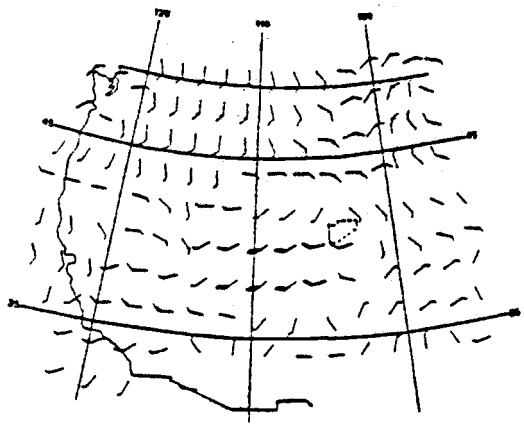

500mb

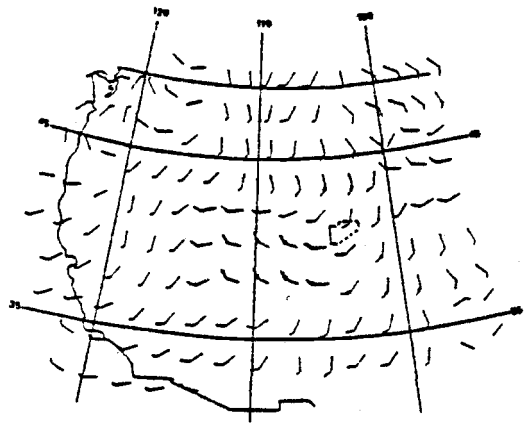

700mb

Figure 13. Perturbation winds at 00Z 29 June 1973 at selected pressure levels. Wind barbs same as Fig. 12. Dashed area is outline of NHRE network.

trough location is seen. Wind profiles for earlier time periods (not shown) also exhibit the perturbation vortex only at 300 and 400 mb, but by 12Z 29 June the vortex is seen to weaken at 300 mb and become clearly visible from 400 to 700 mb.

The technique used in the determination of $\bar{\tilde{V}}$ and $\tilde{V}'$ can result in problems if there is a trend in the large scale data. In such a case, the computed fixed mean may give meaningless perturbation values, particularly at the boundary time periods. A better method for estimating the perturbations would be to use a floating mean, in which the mean for a particular time period is obtained by averaging data from the times immediately before and after. Since the 300 mb contour patterns showed little change through the two days, and because of the exploratory nature of this technique, it was felt justified to use the simple time mean. Perturbation vortex continuity of structure and movement support this supposition, especially during the important interior times.

Temperature and height perturbations were not investigated in this same manner because unlike winds aloft, they are subject to substantial diurnal changes (Teweles, 1949). They can, however, be estimated through use of the wind field. Winds above the boundary layer are approximately geostrophic; hence, streamlines will show the contour structure. The thermal structure can be deduced from vertical wind shear.

VI. DYNAMICAL FORCING

Dynamical forcing refers to a forced lifting process generated through the vertical distribution of synoptic scale divergence. Upper level divergence coupled with lower level convergence typically forces upward motions at intermediate levels. Quantitative estimates of the large-scale vertical velocity can be computed by integration of the equation of continuity, equation (6), i. e., integrating the divergence between pressure levels. These vertical motions are important because of their ability to reduce the atmospheric static stability. The weakening or elimination of a low level inversion for example, may result from such forcing. To study this dynamical forcing, divergences, given by

$$DIV = \left(\frac{\partial u}{\partial x} + \frac{\partial v}{\partial y}\right)_p \qquad (9)$$

at surface and selected mandatory pressure levels (700, 500, 400, 300 mb) were calculated using u and v component finite differencing from the Barnes objective analysis grid network.

Winds obtained from surface weather reports were used to calculate the low level divergence. However, these surface divergences are not always representative of low level divergence because surface winds are subject to topographical influences. To minimize this error, only surface winds from the relatively smooth

area east of the Rocky Mountains were used, unfortunately limiting the area of investigation.

Surface wind components at twenty-five points on a 1^{o} latitude-longitude grid were differenced over a 2^{o} distance to obtain horizontal divergence at nine grid points. The small size of this grid makes the grid center the most representative of the area divergence, as it has the least boundary influences. The central point lies 50 km southeast of the NHRE network, but due to similar terrain, it should have similar environmental conditions. Table 3 lists the divergence values at the grid center for indicated times on 27 and 28 June 1973.

Table 3. Surface divergence values for Eastern Colorado. Values are x 10^{-6} sec^{-1}.

Time	27 June 1973	28 June 1973
12Z	- 2	-13
15Z	- 4	-13
18Z	- 1	-17
21Z	- 8	-12
22Z	+10	-11
23Z	-21	-14
24Z	-17	- 4

In Table 3, the convergence values on 27 June remain low through the early afternoon, suggestive of little or no organized convection, but increase to -21×10^{-6} sec^{-1} by 23Z. This relates well with hourly surface reports from Akron, the closest station to the grid point. Here only a few cumulus clouds were reported through the afternoon, but with towering cumulus in all quadrants at 24Z. Convergence values on 28 June were generally higher through the day than those of 27 June. This kind of steady low level convergence is associated with gentle rising motions of a few cm/sec leading to static instability. Akron reports a few cumulus through the afternoon of the 28th with a thunderstorm occurring at 24Z.

If the perturbation vortex moving through Colorado the afternoon of the second day is to have an effect on the environment, its role would be to reduce the static stability through large-scale divergence at upper levels and convergence at lower levels in advance of the perturbation vortex (see Appendix). Consequently, perturbation wind components on a 2° latitude-longitude grid were differenced over a 4° interval centered about the grid point to compute perturbation divergences at 700, 500, 400 and 300 mb levels for the five time periods. These perturbation divergences, however, approximate the actual wind divergences because the divergence of the mean wind (Figure 14) is small, confirmed by analyses not shown.

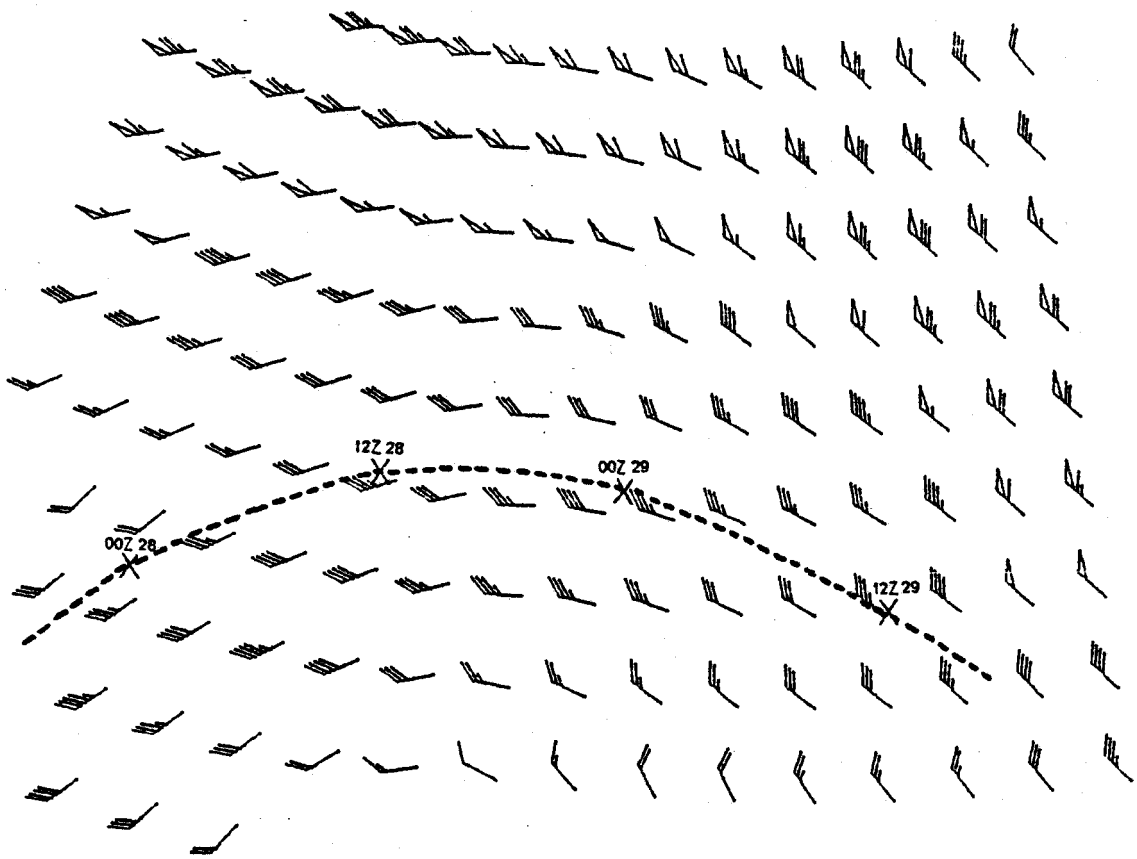

Figure 14. Mean 300mb winds, and 300mb vorticity maximum track at indicated times.

Unfortunately a short balloon flight at station 583 (Winnemucca, Nevada) on 12Z 29 June 1973 flawed the mean and perturbation winds above 500 mb in the region of station 583. Perturbation plotted winds were not noticeably affected, but the perturbation divergences being more sensitive displayed an aberration. Therefore, all 300 and 400 mb divergences, plus the 700 and 500 mb divergences at 00Z 29 June were recomputed using observed wind data. Perturbation wind and observed wind divergence comparisons show quite similar patterns for all levels at all time periods except at 300 mb on 00Z 28 June, when the vortex was over station 583. For the 300 mb levels, it was deemed more appropriate to use the observed wind divergence.

The two most important aspects to be seen on the observed wind divergence maps are: (1) The divergence-convergence couplet associated with the migrating perturbation vortex, and (2) the vertical divergence structure in the vicinity of the NHRE network. Figure 15 displays the divergence contours found at 300 mb; Table 4 lists vertical profiles of perturbation divergence utilizing data from the same grid point as used for surface divergences.

Because the perturbation vortex is located off the California coast in an area of no data at 12Z 27 June, the divergence-convergence couplet cannot be identified at this time (not shown). Table 4 shows no organized ascent at this time near the NHRE

network. By the afternoon of the first day at 00Z 28 June, the perturbation vortex is within the data region, and vorticity isolines depict the vortex (Figure 15a). A divergent region can be seen in advance of the vorticity maximum. Convergence behind the vorticity maximum can only be inferred, however, through the negative values to its southwest. Further east of the short wave trough at the NHRE network, a divergence profile at this time (Table 4) shows strong low-level convergence, with little vertical organization.

Table 4. Perturbation divergence values at indicated levels for June 1973, taken at same grid point as Table 3. Surface values are from Table 3, and constant pressure values are from analyses of Figure 15. Values are x 10^{-6} sec^{-1}.

Pressure	12Z 27 June	00Z 28 June	12Z 28 June	00Z 29 June	12Z 29 June
300 mb	+ 2	+ 2	+ 2	+10	- 3
400 mb	- 2	+17	+ 1	-26	+ 9
500 mb	+14	- 3	- 5	-23	+16
700 mb	+ 9	+ 7	+ 3	-24	+ 6
SFC	- 2	-17	-13	- 4	

Twelve hours later at 12Z 28 June, the vortex has moved several hundred miles to the northeast and exhibits a weakening in the divergence couplet (Figure 15b). This weakening may be due to vertical shrinking as the system passes over the high western plateau. This results from the conservation of potential vorticity during

(a)

00Z
28 June

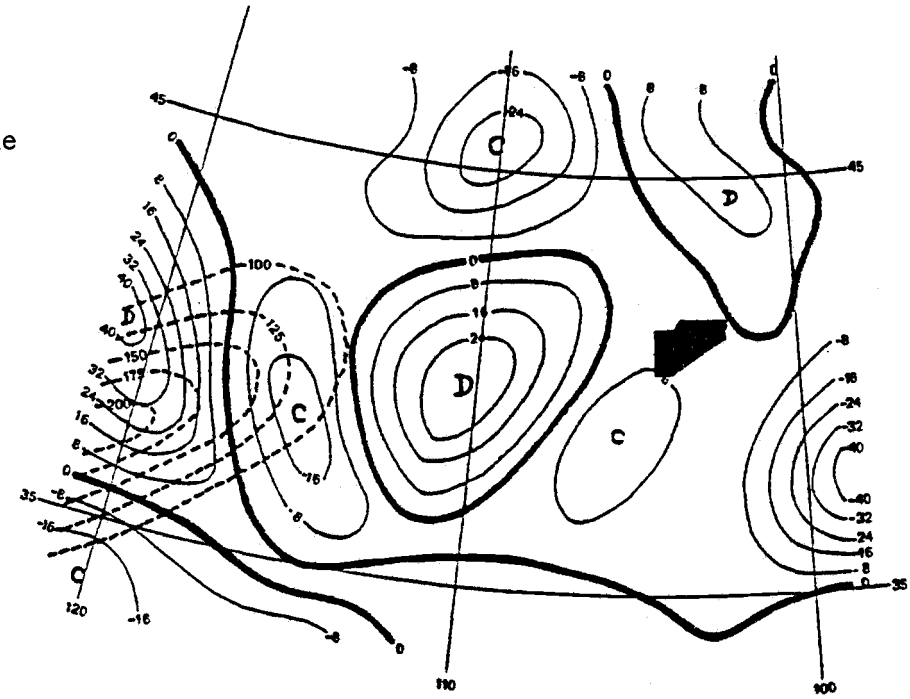

(b)

12Z
28 June

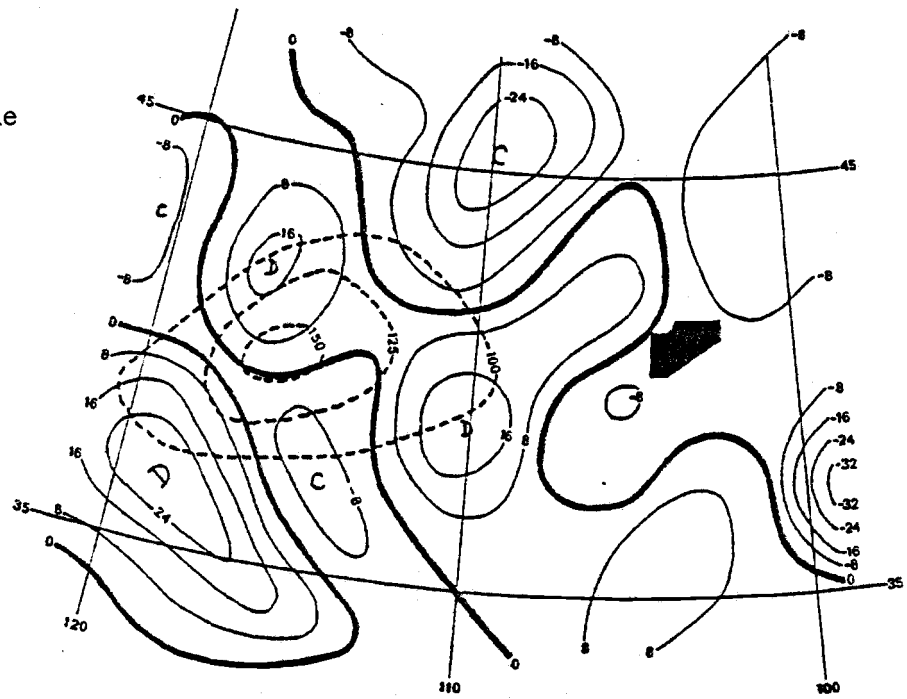

Figure 15. Observed wind divergences and vorticity at 300mb at respective times during June 1973. Solid lines are divergence and dashed lines are vorticity, values are x10-6s-1. Letters C and D denote centers of convergence and divergence. Shaded area indicates NHRE network.

(c)
00Z
29 June

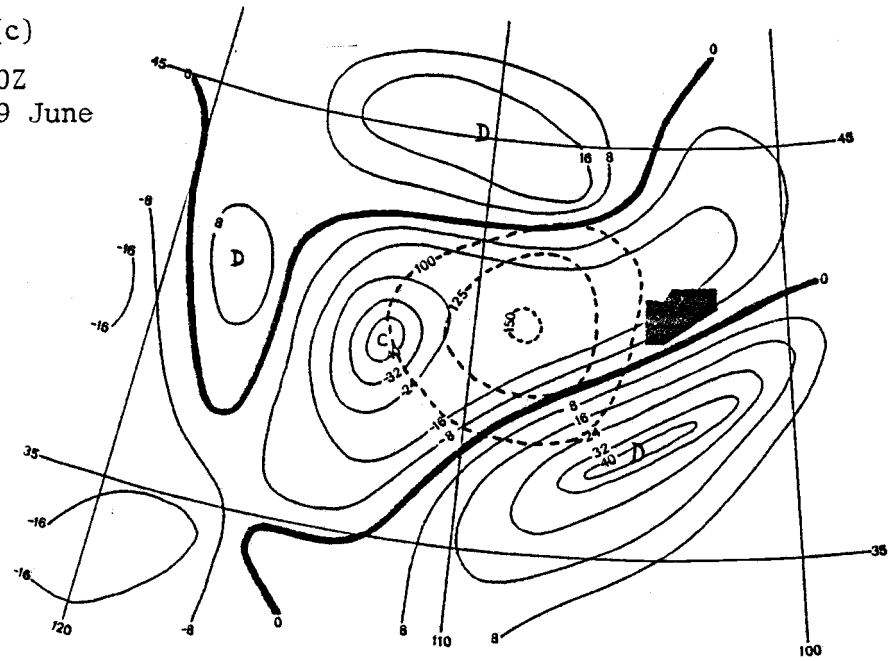

(d)
12Z
29 June

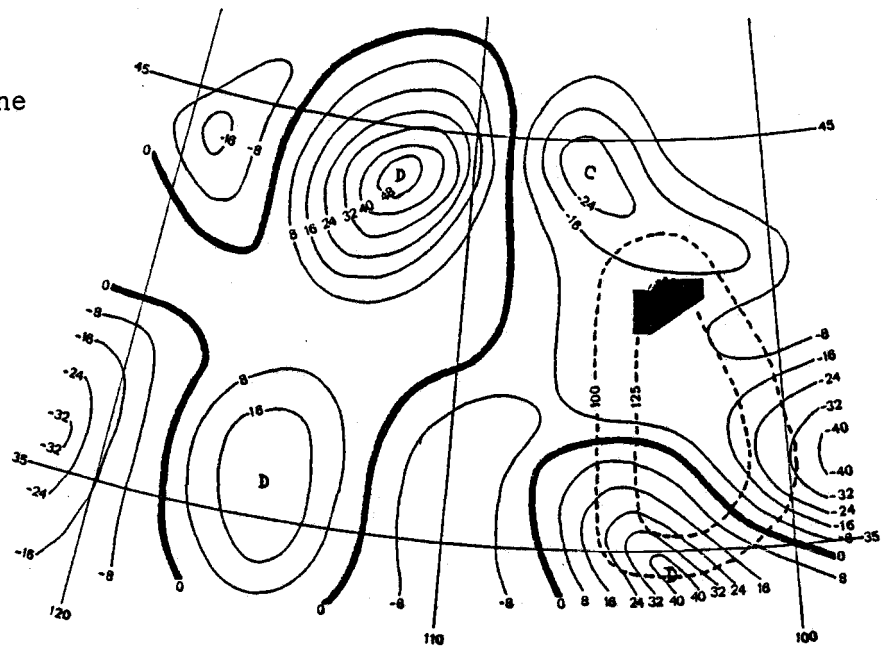

Figure 15 continued

adiabatic motion. At this time at 300 mb the NHRE network lies just to the east of the approaching divergent region. Table 4 reveals the beginning of a convergent trend in the perturbation divergence structure at the NHRE network at 700, 500, and 400 mb.

By the following morning, 12Z 29 June, an apparent weakening of the system can be seen at 300 mb in Figure 12d. This is reflected in the divergence analysis (Figure 15d) which shows considerable complexity. Figure 17a reveals the perturbation vortex to be well organized at 400 mb at this time, with 17b exhibiting the divergence-convergence couplet in good alignment with the vorticity pattern and the mean wind.

The vortex center has migrated into Colorado by the afternoon of the second day and at 00Z 29 June exhibits a strengthening of the couplet divergence gradient (Figure 15c). Perturbation divergences at selected pressure levels are also shown for this time (Figure 16). Note the positioning of the 700 mb convergence-divergence couplet below the respective 300 mb divergence-convergence couplet, as expected from the Dines' compensation principle. The 500 and 400 mb levels display the transition between upper and lower level divergences. Figure 16 and the surface divergence values from Table 3 show strong convergence up through 400 mb with convergence at 300 mb in the vicinity of the NHRE network during the afternoon of the 28th (summarized in Table 4 for 00Z 29 June). Although quantative estimates of

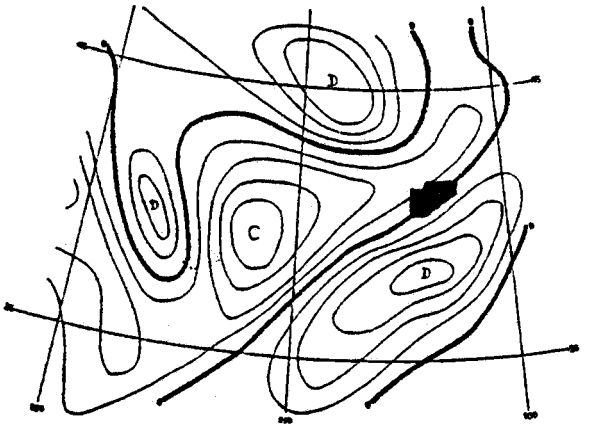

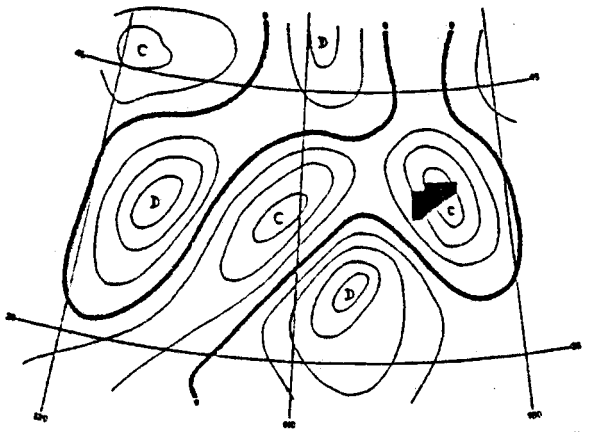

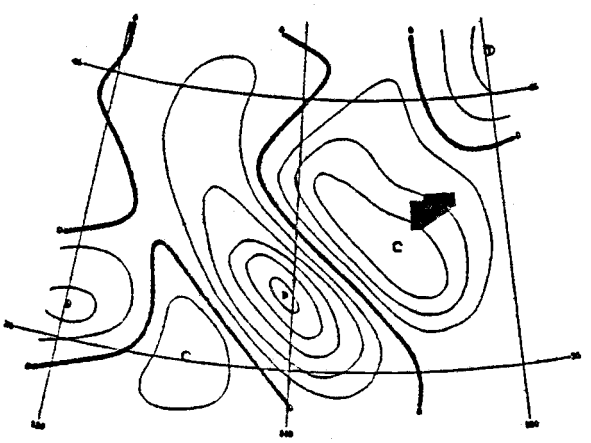

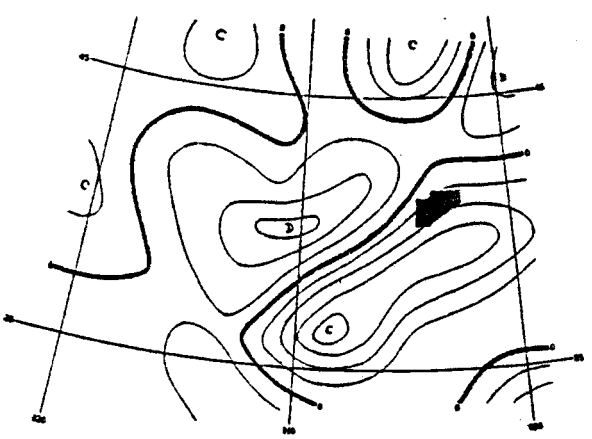

Figure 16. Perturbation divergences at selected levels at 00Z 29 June 1973. Divergence isolines are every $8 \times 10^{-6} s^{-1}$. Shaded area is the NHRE network. The letters C and D refer to convergent and divergent regions respectively.

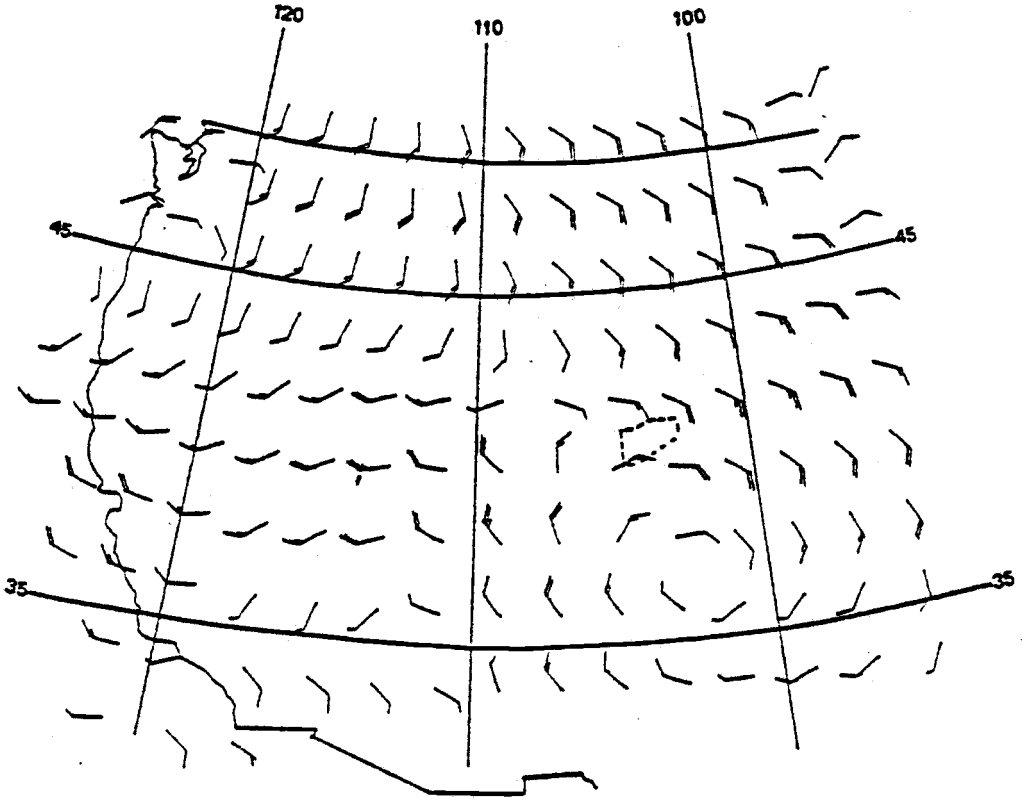

Figure 17a. 400mb perturbation winds on 12Z 29 June 1973. Wind barbs are in tens of kts. Dashed area is the outline of the NHRE network.

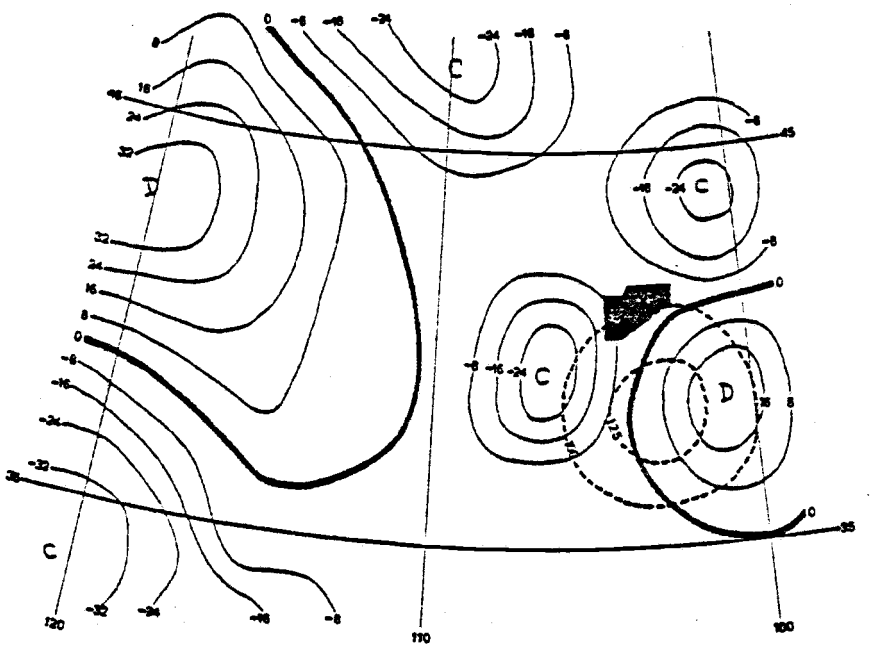

Figure 17b. Observed wind divergences at 400mb on 12Z 29 June 1973. Divergences are $x10^{-6}s^{-1}$. See Figure 15 for symbol definitions.

vertical velocity may not be possible from this analysis, the continuity equation (Equation 6) affirms that there must be vertical motions occurring. These vertical motions can lead to the release of instability. Similar studies by MacDonald (1977) and Ninomiya (1971) have found areas of deep convection to have convergence through the middle troposphere (400 mb).

The divergence structure through the two day period was more complex than usually found in textbook models. There was some speculation whether a smoothing technique might improve the analysis. A spatial smoothing was done by creation of new grid points through an averaging of the four surrounding divergence grid points. This slightly changed the values but not the pattern of the divergences. Another technique involved recomputing new wind components using smoother Barnes analysis weighting factors and then calculation of new divergences from these. Again the smoothed analyses showed little difference from the original analyses, thus giving a certain credibility to the latter. Other investigators have found a similar complexity in the divergence structure. Published perturbation divergence patterns by Reed et al. (1977) show tropical easterly waves to have a complex structure. Kung (1973) displays smoothed vertical velocity profiles for the United States for one day which had very irregular associated divergence profiles.

The track of the 300 mb vorticity maximum (Figure 14),

corresponding with the vortex center, very closely follows a mean-wind streamline. It moved at 20-25 kts, the mean 700-300 mb wind speed, demonstrating that the perturbation vortex behaves like a disturbance carried in the mean flow.

The difficulty in following the details of the divergence patterns between maps is a combination of the following factors:

(1) Systems may wax and wane rapidly and can show substantial changes between 12 hour observations.

(2) Atmospheric flow is largely geostrophic with small divergence values. Inaccuracies in the wind observations can often be as large as the divergence values computed from them.

(3) Transition divergence levels (near 500 mb in this case study), where the divergence is changing sign and small, are often too weak to show any clear patterns.

(4) Since constant pressure surfaces are nearly horizontal, they may not be the best way to follow divergence patterns which may have considerable tilt.

In spite of these problems, significant information can be obtained from such an analysis. The analysis shows little organized divergence structure on 27 June 1973 over the NHRE network. By the afternoon of 28 June 1973, the approach of a perturbation vortex (short wave trough) and its accompanying divergence structure produce strong upper level divergence superimposed over a deep

layer of convergence above the NHRE network, leading to dynamical lifting of the potentially unstable layer at the top of the mixed layer and release of instability.

An attempt was made to obtain quantitative estimates of the vertical velocity in pressure coordinates (ω) above the NHRE network through the two day period. A method based on the mass budget was used to calculate an area-mean omega ($\overline{\omega}$) for 25 mb thick vertical layers. The mean omega defined by $\overline{\omega} = \frac{1}{A}\iint \omega dA$ is differentiated with respect to pressure

$$\frac{\partial \overline{\omega}}{\partial p} = \frac{1}{A}\iint \frac{\partial \omega}{\partial p}\, dA$$

By use of the continuity equation (Equation 6), this becomes

$$\frac{\partial \overline{\omega}}{\partial p} = \frac{1}{A}\iint -\tilde{\nabla}\cdot\tilde{V} dA$$

and

$$\frac{\partial \overline{\omega}}{\partial p} = \frac{1}{A}\oint -\tilde{V}\cdot\tilde{n} dL$$

Integration upward through a layer p_1 to p_2, and rearrangement of terms gives

$$\overline{\omega}_2 = \frac{1}{A}\left[\overline{\omega}_1 A + \int_{p_1}^{p_2}\oint -\tilde{V}\cdot\tilde{n} dL dp\right] \qquad (10)$$

Where $\tilde{n}$ is the outward directed unit normal to L, and L is the boundary of the area A. Hence, the mean vertical velocity ($\overline{\omega}_2$) at

pressure p_2 is equal to the sum of the mass flux up through the lower pressure surface and the mass flux in through the sides of the layer, all divided by the cross-sectional area. In this case, the cross-sectional area is defined by a pentagon formed by the five NHRE radiosonde stations (Figure 18). The only winds used were those taken at the vertex stations, and these were "heavy smoothed" (NHRE radiosonde computer printout sheets) in the vertical at each station. Inherent in the method is the assumption of linearity in the wind field between stations.

The initial $\bar{\omega}$ used in Equation 10 is non zero, a consequence of the sloping terrain within the NHRE network. Its determination may be demonstrated through the use of Figures 18 and 19. The pentagon formed by the five NHRE radiosonde stations (Figure 18) may be extended upward to form a truncated right pentagonal prism. An unfolded view of the sides of this prism, bounded by the ground and the pressure of the highest elevation station (Grover), illustrates a number of triangles and rectanges fitted to this surface (Figure 19). Using these areas and winds linearly interpolated to requisite pressures at each station, the total mass flux into the prism sides is calculated. Finally, the impermeability of the ground requires that the mean omega needed for Equation 10 is the total surface flux divided by the area of the pentagon.

The linearity uncertainty coupled with the inaccuracy of the

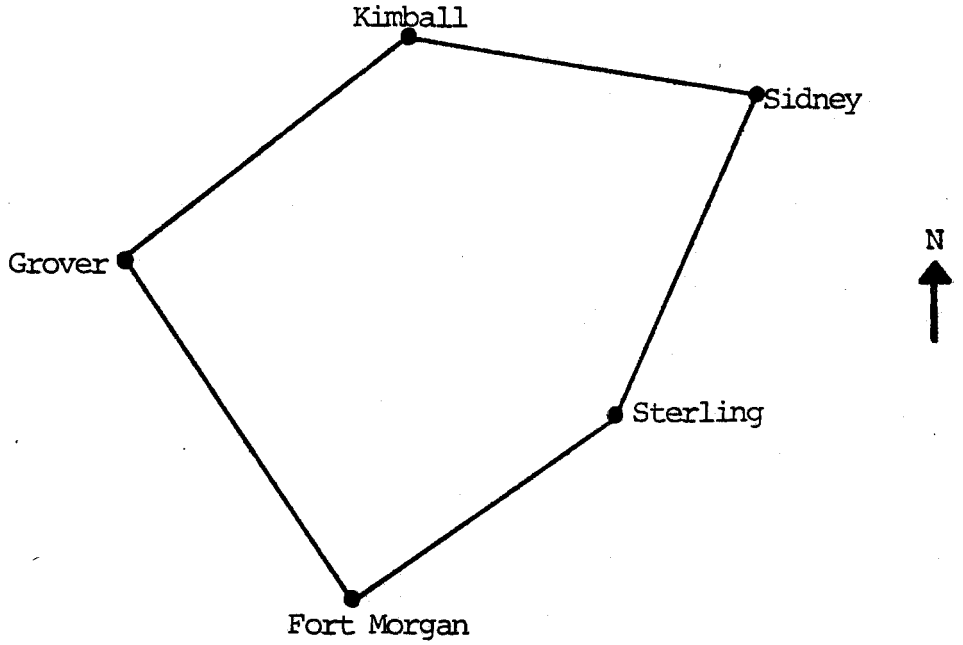

Figure 18. The pentagon formed by the five NHRE radiosonde stations used in the calculation of $\bar{\omega}$, the mean vertical velocity in pressure coordinates.

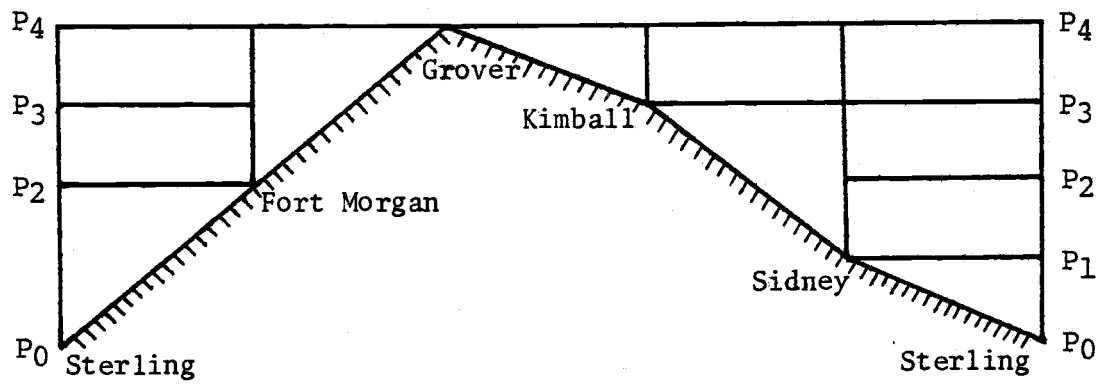

Figure 19. An unfolded view of the sides of a truncated right pentagonal prism, produced by an upward extension of the pentagon formed by the five NHRE radiosonde stations illustrated in Figure 18. Vertical axis is pressure, decreasing with height.

original data will produce errors in the divergence leading to a compounding of errors in the vertical velocity. O'Brien (1970) has suggested a correction scheme to improve vertical velocity profiles by forcing the upward velocity to zero at the tropopause, while making smaller corrections through the intermediate layers. This method was tried and abandoned because it was found that the spurious upper level vertical velocities were so large that the correction overly influenced the low level vertical velocities.

Figure 20 displays mean vertical velocities for an area encompassed by the five NHRE stations. At densities near 10^{-3} g cm^{-3}, a negative microbar per second is associated with an upward velocity of one centimeter per second. The strong vertical motions near the tropopause level (near 200 mb) on both days reveal an error in the analysis. This is due in part because these calculations assumed the area enclosed by the balloons during ascent did not significantly differ from the initial area. But the apparent convergent and divergent layers suggest changes in balloon positions with respect to each other, which would change the computed flux into the sides of the pentagon, and change the cross sectional area used to convert vertical flux into mean vertical velocity. Furthermore, the small scale of the NHRE radiosonde network can only measure a localized divergence, and balloon drift into adjacent small-scale divergent areas may give horizontal fluxes unrepresentative of the NHRE area.

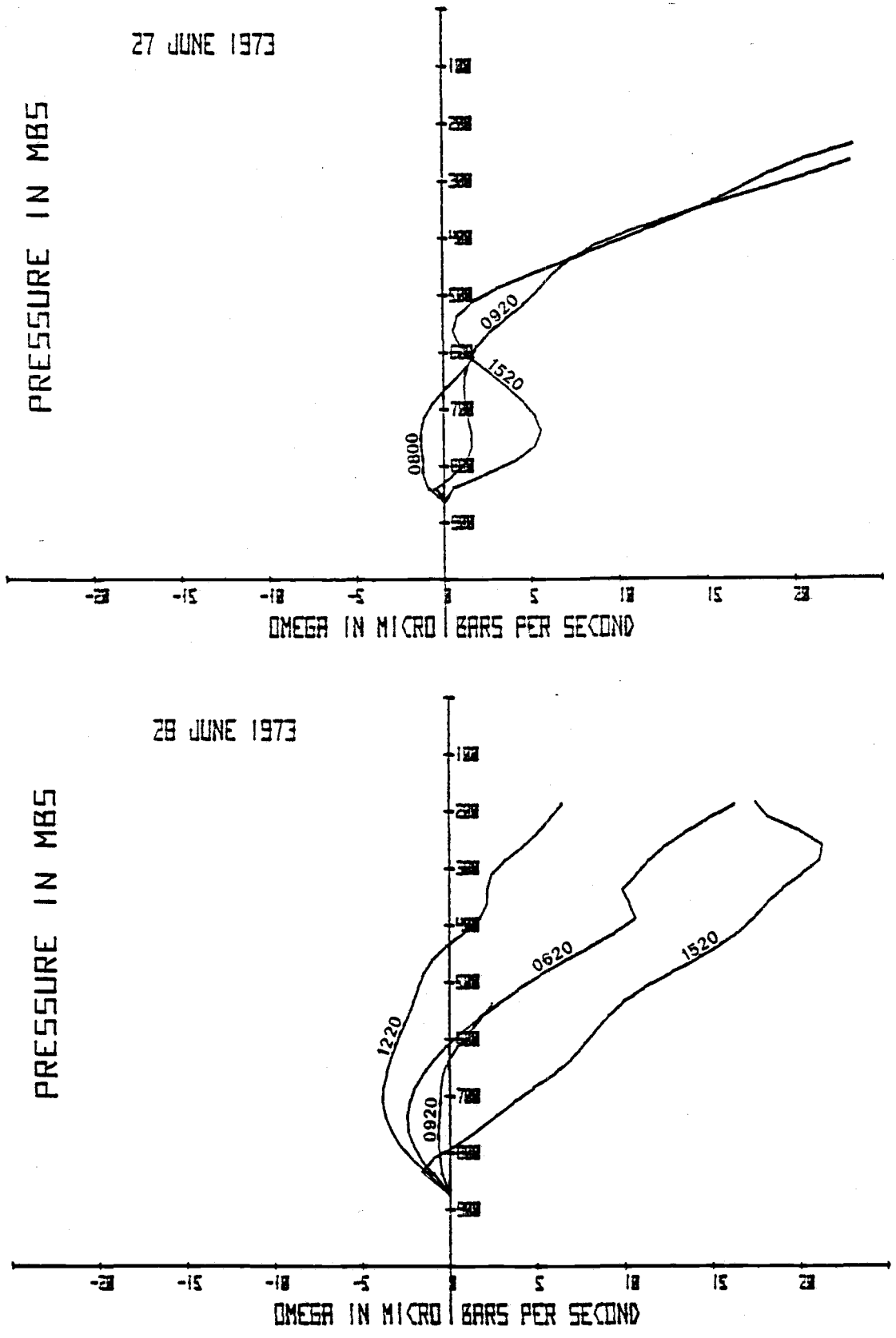

Figure 20. Mean vertical velocities in pressure coordinates for the NHRE network, times are MST.

These problems evidently have introduced a significant error into the analysis which accumulates with height. Therefore only the lower layers should be considered.

Vertical velocities were computed for regions bounded by three and four stations (not shown), with similar results. Since the closer the stations, the greater the effects of turbulent fluctuations and error on the finite wind velocity derivatives between stations, the five-station mean vertical velocities ($\overline{\omega}$) were deemed more accurate because of the larger area encompassed. At 0800 MST on 27 June 1973, Figure 20 displays a low layer of upward accelerations, suggesting convergence by the continuity equation, in good agreement with Table 3 at 15Z, which shows surface convergence. By 0920 MST, the profile suggests even less convergence in the surface layer, in agreement with a decrease in surface convergence between 15Z and 18Z listed in Table 3. The 1520 MST profile shows strong downward accelerations, associated with strong low level divergence, possibly due to frictional effects in the high pressure region over the network at this time. Table 3 shows fair agreement, with surface divergence values between $+ 10 \times 10^{-6} s^{-1}$ and $-21 \times 10^{-6} s^{-1}$. Making allowance for the balloon area error, the convergent layer above the surface layer probably has some associated upward motions at this time. A four-station 1220 MST computation suggested divergence in the friction layer, and very strong convergence

and upward motions above that layer. These afternoon rising motions are decoupled from the surface moisture and perhaps help explain the lack of moist convection observed within the network during the early afternoon on the 27th.

On 28 June, low level convergence and upward motions are evident throughout the day (Figure 20), correlating well with Table 3 which shows surface convergence throughout the day. The vertical velocity profiles exhibit an increase in height and intensity of upward motions from morning to afternoon, in agreement with synoptic scale analyses which show strong upper level divergence passing aloft. By 1520 MST, thunderstorms are already progressing at Grover, resulting in unrepresentative wind data from that stations. The 1520 MST vertical velocity computations should thus be disregarded.

This chapter has attempted to examine the vertical motion field during the two days for some dynamical forcing mechanism, through surface divergences, constant pressure divergences, and vertical velocity profiles. It should be kept in mind that these computed divergences were done on different scales. The NHRE radiosonde network scale was about 60 km, the surface station network separation was about 110 km, and the synoptic radiosonde network scale was about 220 km. Agreement among them has been generally consistent, but differences in values should be expected

because features found through small-scale analysis can easily be lost in a larger-scale analysis. The surface analyses suggest generally stronger low level rising motions on the second day; the constant pressure analyses indicate shallow upward motions the first day and deep organized upward motions the second day; and the vertical velocity profiles show greater low-to-middle level ascending motions on 28 June than 27 June. These strong rising motions on 28 June are clearly associated with the approach of a short wave trough and its accompanying divergence structure.

VII. SATELLITE PHOTOGRAPHS

The conclusion thus far is that the approach of a short wave trough with associated rising motions was instrumental in the release of instability in the region of the NHRE network, resulting in a severe hailstorm. These synoptic scale rising motions are too weak to be measured directly, and throughout this thesis have been determined indirectly through divergence estimates. But qualitative measures of vertical velocity can be made through cloud development. As the short wave trough moves across the country, if rising motions are associated with it, and if enough moisture is available, clouds will form and move with the disturbance. There are some problems though in this type of analysis: (1) Some of the clouds may be orographically generated and have nothing to do with the short wave, and (2) the air may be too dry to exhibit clouds. The following satellite photographs may show the movement of a short wave trough induced cloud system.

Figure 21 shows IR satellite photographs taken from 09L 26 June 1973 to 09L 27 June 1973. The early sequence of photos reveals a band of clouds moving inland from the Pacific Ocean, following an anticyclonic path. By 09L 27 June there is a considerable anticyclonically directed cloud streak across central California. Upper air maps at this time show the short wave to be in the vicinity of the central California coast. With ascent ahead of the trough, lifting

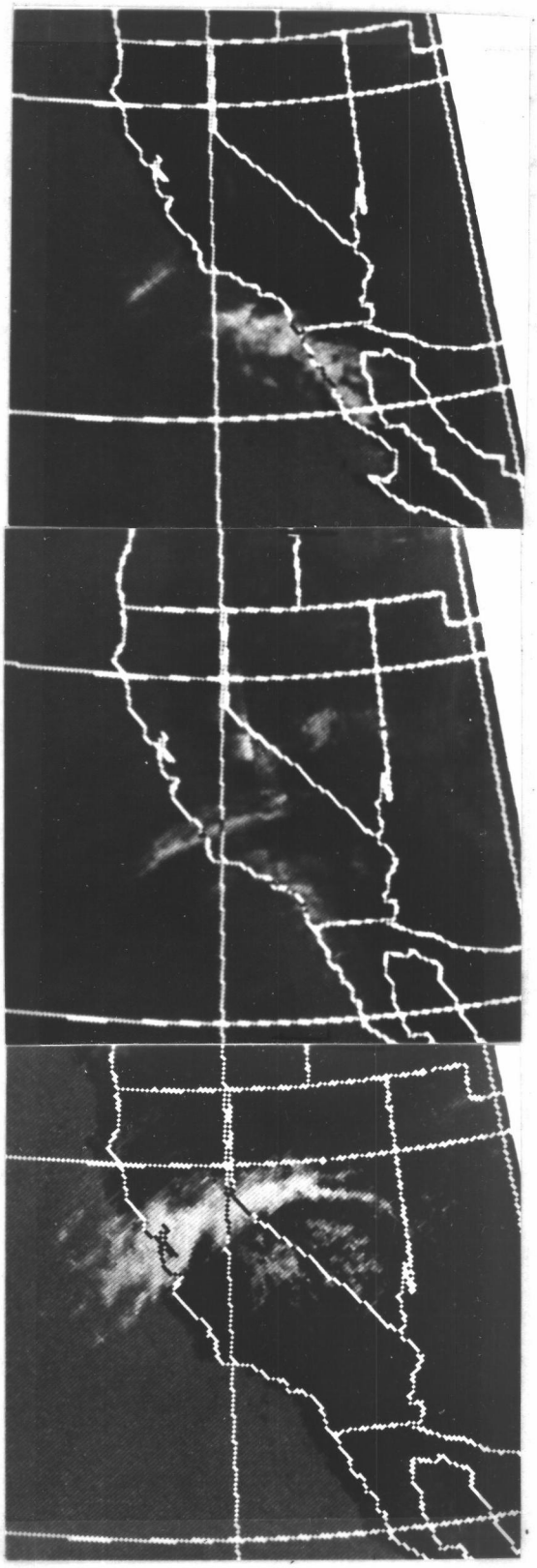

(a) 09L 26 June 1973

(b) 21L 26 June 1973

(c) 09L 27 June 1973

Figure 21. This sequence of IR photographs shows from (a) to (c) a band of clouds moving inland and northeastward from the Pacific from 09L 26 June to 09L 27 June 1973.

will bring the warm moist coastal air to saturation, and the flow downstream of the trough may be advecting the clouds inland anticyclonically.

Figure 22 shows satellite photographs from 21L 27 June 1973 to 21L 28 June 1973 with superimposed divergence patterns, vorticity maxima (v) and trough locations. Since map times do not correspond with other data times, it has been necessary to interpolate the dynamic and synoptic features to the map times. Figure 22 at 21L 27 June shows the 300 mb observed wind divergence couplet exhibiting good agreement with the vorticity maximum location (v) and the clouds. Although the structure of the short wave is difficult to define at this time, its location relates fairly well with the cloud areas. The short wave becomes more evident by 09L 28 June, with the 300 mb trough exhibiting a classical example of upper level divergence on the downwind side and convergence on the upwind side of the trough. The clouds, although scattered, show good correspondence with the divergent region. By 21L 28 June, a large region of cloudiness can be seen east of the Rocky Mountains, in part due to the perturbation vortex associated large divergent region aloft. Again, good correlation among vorticity maximum, trough portion, divergence couplet location, and clouds can be seen.

A visual satellite photograph at 09L 29 June 1973 (Figure 23) shows the 300 mb divergence in a region of cloudiness, but the short

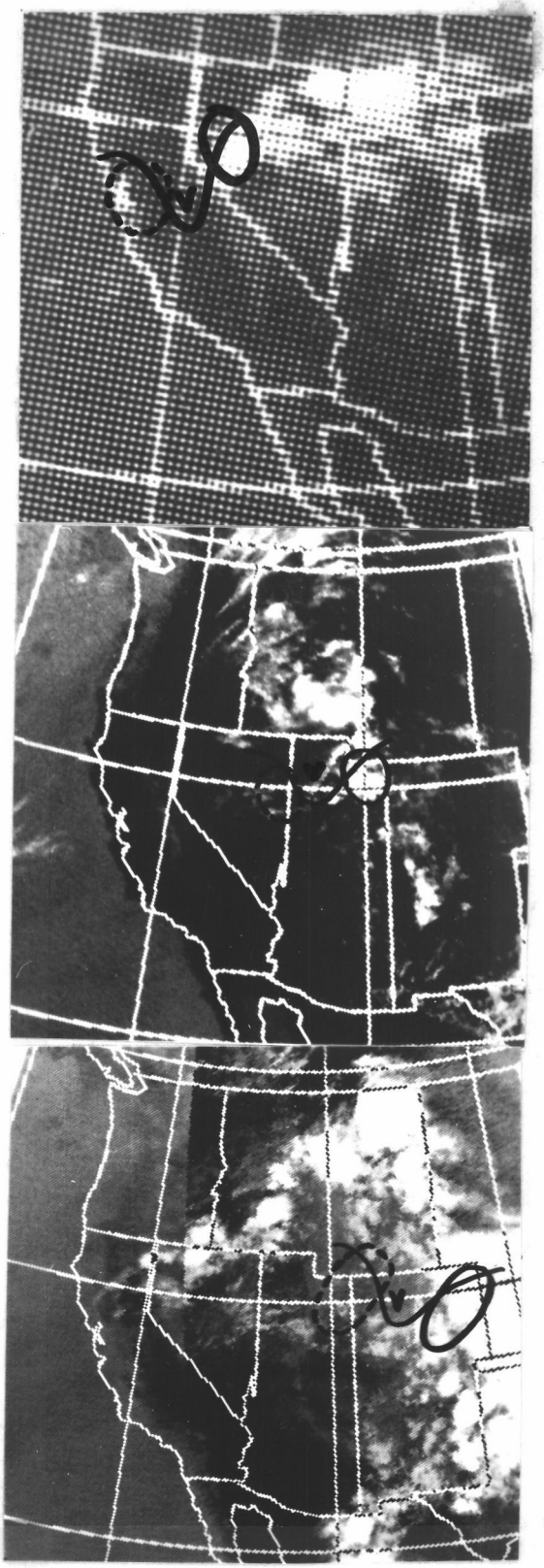

21L 27 June 1973

09L 28 June 1973

21L 28 June 1973

Figure 22. IR photographs from 21L 27 June to 21L 28 June 1973 with superimposed 300mb trough, convergence region (dashed area), divergence region (solid area) and vorticity max region. Note the good cloud and 300mb divergence correlation.

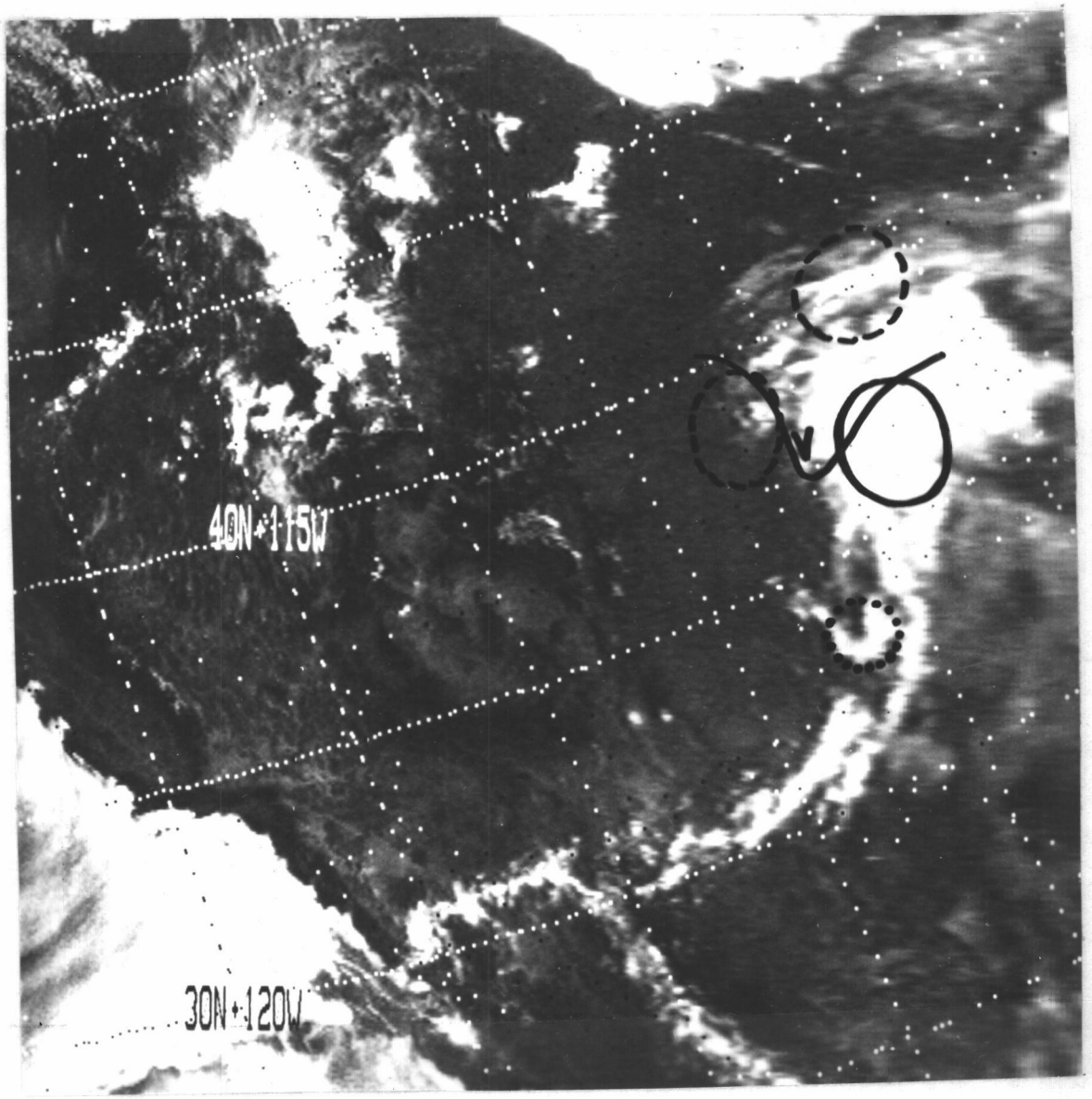

Figure 23. Visual satellite photograph at 09L 29 June 1973. Displayed are 300mb trough, 400mb convergent region (dashed area), 400mb divergent region (solid area), 400mb vorticity maximum location, and 300mb divergent region (dotted area). Notice the upper-level trough is not associated with the 300mb divergence region at this time.

wave trough and main cloudiness are related to the 400 mb divergence region. This relates well with Figures 15 and 17 which show the 300 mb divergence maximum in that region to be unrelated to the short wave trough.

In general, there seems to be good agreement between the moving short wave and the cloud system; and between computed upper level divergence regions and clouds.

VIII. SUMMARY

This case study has attempted to exhibit the changes in atmospheric conditions over the two day period 27-28 June 1973, leading up to a severe hailstorm within the NHRE network during the late afternoon of 28 June. Although routine surface and upper air maps on the morning of 28 June displayed no apparent evidence of approaching severe weather, careful analyses have shown that the important changes were synoptically induced. The principal changes were: (1) Increased low level moisture on the second day and (2) a short wave trough passage on the second day which provided the lifting mechanism to initiate the hailstorms.

The above average low level moisture of 28 June appears to be due primarily to an influx of moisture with the southeast winds, a result of the strengthened surface pressure gradient force associated with the approach of the short wave. The thinner mixed layer on this day further contributed to the maintenance of high moisture values by reduction of dry air entrainment into the moist layer. Although evaporation effects are difficult to quantify, estimates show that it is a definite factor in the moisture budget even in this semi-arid region. The high moisture content had the effect of decreasing the static stability on 28 June and creating a potentially unstable layer at the top of the mixed layer.

The static stability was further decreased by upper level cooling (shown at 400 mb) which was associated with the approach of a short wave trough. With careful analysis, a short wave trough could be detected moving across the western U.S., following the contours of a high pressure ridge situated aloft. Due to the weakness of the trough, a perturbation wind analysis was used to emphasize its existence. The analyses revealed a vortex in the perturbation winds with a track closely approximating a streamline of the mean winds. Constant pressure maps of divergence of observed winds and divergence of perturbation winds showed a divergence-convergence couplet to be associated with the perturbation vortex (short wave trough).

The trough approach brought about a strengthening of the surface convergence within the NHRE network on 28 June, deepening to 400 mb by the late afternoon. Estimates of vertical velocities over the NHRE network suggest subsidence on the first day, while revealing low level convergence and rising motions on the second day. These rising motions can assist in the release of the potential instability.

Satellite photographs were used to give qualitative direct evidence of rising motions associated with the moving short wave trough. The photographs showed good agreement among trough locations, divergence couplets, vorticity maxima, and clouds.

These analyses have shown that for the forecasting of weak summertime systems, the 500 mb surface is too low to be effective; the 300 mb surface seems to be better. Furthermore, perturbation wind analysis appears to be a good technique to emphasize these weak systems.

Future work in this area should include a comprehensive program of evaporation measurement. It is too important a variable to be ignored in hailstorm research. Additional vertical velocity computations using synoptic network constant pressure divergences at 50 mb intervals should be made and compared with other techniques such as the omega-equation.

BIBLIOGRAPHY

Anderson, C. E., and L. W. Uccellini, 1973: Studies of meteorological factors involved in the formation of severe local storms in the Northeast Colorado Region. Preprints, Eighth Conf. Sev. Local Storms, Denver, Col., Amer. Meteor. Soc., 84-88.

Baldwin, J. L., 1973: Climates of the United States. U. S. Dept. of Comm., Washington, D. C. p. 82.

Barber, D. A., 1973: The production of available thunderstorm energy. Ph.d thesis. University of Wisconsin, Madison, Wisconsin. 83 pp.

Barnes, S. L., 1973: Mesoscale Objective map analysis using weighted time-series observations. NOAA Technical Memorandum ERL NSSL-62. 60 pp.

_____, 1974a: Synoptic-scale environment of Oklahoma thunderstorms, April 29-30, 1970. Papers on Oklahoma thunderstorms, April 29-30, 1970. NOAA Technical Memorandum ERL NSSL-69. 1-16.

_____, 1974b: Mesonetwork observations and analyses. Papers on Oklahoma thunderstorms, April 29-30, 1970. NOAA Technical Memorandum ERL NSSL-69. 17-88.

Beebe, R. G., 1958: Tornado proximity soundings. Bull. Amer. Meteor. Soc., 39, 195-201.

Beebe, R. G., and F. C. Bates, 1955: A mechanism for assisting in the release of convective instability. Mon. Wea. Rev., 83, 1-10.

Beers, N. R., 1945: Atmospheric stability and instability: Slice method. Handbook of Meteorology, McGraw-Hill Book Co., U.S.A., 693-725.

Braham, R. R. Jr., 1952: The water and energy budgets of the thunderstorm and their relation to thunderstorm development. J. of Meteor., 9, 227-242.

Booker, D. R., 1963: Modification of convective storms by lee waves. Meteor. Monogr., 5, No. 27, 129-140.

Browning, K. A., J. C. Frankhauser, J. P. Chalon, P. J. Eccles, R. G. Strauch, F. H. Merrem, D. J. Musil, E. L. May and W. R. Sand, 1976: Structure of an evolving hailstorm, part V: Synthesis and implications for hail growth and hail suppression. Mon. Wea. Rev., 104, 603-610.

Browning, K. A., and F. H. Ludlam, 1962: Airflow in convective storms. Quart. J. Roy. Meteor. Soc., 88, 117-135.

Byers, H. R., and R. R. Brahm, 1949: The Thunderstorm. Washington, D. C., U. S. Govt. Printing Office, 287 pp.

Carlson, T. N., and F. H. Ludlam, 1968: Conditions for the occurrence of severe local storms. Tellus, 20, 203-226.

Ellrod, G. P., and J. D. Marwitz, 1976: Structure and interaction in the subcloud region of thunderstorms. J. Appl. Meteor., 10, 1083-1091.

Environmental Data Service, 1973: Northern Hemisphere data tabulations. Dept. of Comm., National Climate Center, Asheville, North Carolina.

Fankhauser, J. C., A. C. Modahl, C. G. Mohr and M. E. Solak, 1976: Final report--National Hail Research Experiment Randomized Seeding Experiment 1972-1974. Volume III, Meteorological Summary, National Center for Atmospheric Research, Boulder, Colorado, 138-142.

Fawbush, E. J., R. C. Miller and L. G. Starrett, 1951: An empirical method of forecasting tornado development. Bull. Amer. Meteor. Soc., 32, 1-9.

Finley, J. P., 1890: Tornadoes. Amer. Meteor. Jour., 1, 165-179.

Fleagle, R. G., and J. A. Businger, 1974: An Introduction to Atmospheric Physics. Academic Press, Inc., London, pp. 43-45.

Foote, G. B., and J. C. Fankhauser, 1973: Air flow and moisture budget beneath a northeast Colorado hailstorm. J. Appl. Meteor., 12, 1330-1353.

Fujita, T., 1963: Analytical mesometeorology: A review. Meteor. Monogr., 5, No. 27, 77-125.

Galway, J. G., 1956: The lifted index as a predictor of latent instability. Bull. Amer. Meteor. Soc., 37, 528-529.

Hess, S. L., 1959: Introduction to Theoretical Meteorology. Holt, Rinehart and Winston, New York. pp. 51-58.

Holton, J. R. 1973: An Introduction to Dynamic Meteorology. Academic Press, Inc., London, pp. 31, 57, 77-78.

Kung, E. C., 1973: Note on design of an optimized computation scheme for kinematic vertical motion fields. Mon. Wea. Rev., 101, 685-690.

Ludlam, F. H., 1963: Severe local storms: A review. Meteor. Monogr., 5, No. 27, 1-30.

MacDonald, A. E., 1977: On a type of strongly divergent steady state. Mon. Wea. Rev., 105, 771-785.

Mahrt, L., 1975: The influence of low level vertical gradients of moisture on parcel stability. Preprints, Ninth Conf. Sev. Local Storms, Norman, OK., Amer. Meteor. Soc., 40-44.

_____, 1976: Mixed layer moisture structure. Mon. Wea. Rev., 104, 1403-1407.

_____, 1977: Influence of low level environment on severity of High Plains moist convection. Mon. Wea. Rev., 105, 1315-1329.

Marwitz, J. D., 1972a: The structure and motion of severe hailstorms. Part I: Supercell storms. J. Appl. Meteor., 11, 166-179.

_____, 1972b: The structure and motion of severe hailstorms. Part II: Multicell storms. J. Appl. Meteor., 11, 180-188.

_____, 1972c: The structure and motion of severe hailstorms. Part III: Severely sheared storms. J. Appl. Meteor., 11, 189-201.

Miller, R. C., 1967: Notes on Analysis and Severe-Storm Forecasting Procedures of the Military Weather Warning Center, Technical Report 200, Air Weather Service, United States Air Force, Kansas City, Kansas, 82 pp.

Newton, C. W., 1963: Dynamics of severe convective storms. Meteor. Monogr., 5, No. 27, 33-58.

_____, 1966: Circulations in large sheared cumulonimbus Tellus, 18, 699-713.

_____, 1967: Severe convective storms. Adv. in Geophys., 12, 257-306.

Ninomiya, K., 1971: Dynamical analysis of outflow from tornado-producing thunderstorms as revealed by ATS III pictures. J. Appl. Meteor., 10, 275-294.

NOAA, National Weather Service Operation Manual, 1977. U.S. Dept. of Comm., Washington, D. C., Part C, Chapter 40, p. 4.

Normand, C. W. B., 1946: Energy in the atmosphere. Quart. J. R. Meteor. Soc. 72, 145-167.

O'Brien, J. J., 1970. Alternative solutions to the classical vertical velocity problem. J. Appl. Meteor., 9, 197-203.

Palmen, E., and C. W. Newton, 1969: Atmospheric Circulation Systems: Their Structure and Physical Interpretation. Academic Press, Inc., London, pp. 300-425.

Palmer, W. C., and A. V. Havens, 1958: A graphical technique for determining evapotranspiration by the Thornthwaite method. Mon. Wea. Rev., 86, 123-128.

Penman, H. L., 1948: Natural evaporation from open water, bare soil and grass. Proc. Roy. Soc. London, A193, 120-145.

Petterssen, S., 1956: Weather Analysis and Forecasting, Second Edition, Volume I: Motion and Motion Systems. McGraw Hill Book Co., U.S.A., p. 323.

Reed, R. J., D. C. Norquist and E. E. Rechker, 1977: The structure and properties of African wave disturbances as observed during phase III of GATE. Mon. Wea. Rev., 105, 317-333.

Renne, D. S., 1969: Stability and dynamic processes in the formation of High Plains hailstorms. Atmos. Sci. Paper No. 136, Colorado State Univ., 53 pp.

Rossby, C. G., 1932: Thermodynamics applied to air mass analysis. MIT, Meteor. Papers, 1, 60 pp.

Stommel, H., 1947: Entrainment of air into a cumulus cloud. J. of Meteor., 4, 91-94.

Tweles, Sidney, Jr., 1949: The tentative normal diurnal height change of the 700-millibar surface over the United States and adjacent areas. Mon. Wea. Rev., 77, pp. 167-175.

Whitney, L. F. Jr., 1977: Relationship of the subtropical jet stream to severe local storms. Mon. Wea. Rev., 105, 398-412.

U. S. Weather Bureau, 1964: Climatography of the United States, No. 86-5. Decennial census of United States Climate--Climatic summary of the United States--Supplement for 1951 through 1960; Colorado and Nebraska. U. S. Govt. Printing Office, Washington, D. C., 57-60.

Wyoming State Climatologist, estimated 1964: Normals of evapotranspiration (in inches) in Wyoming. U.S. Dept. Commerce, Casper, Wyo., 15 pp.

APPENDIX

APPENDIX

Perturbation Vortex Divergence Patterns

This section will explain why there is a divergence-convergence couplet associated with the perturbation vortex. A simplified form of the vorticity equation in pressure coordinates, excluding tilting and friction terms, can be written as (Holton, 1973)

$$\frac{d}{dt}(\zeta + f) = -(\zeta + f)\tilde{\nabla}_p \cdot \tilde{V}$$

By expansion of the left side:

$$\underset{(1)}{\frac{\partial \zeta}{\partial t}} + \underset{(2)}{\frac{\partial f}{\partial t}} + \underset{(3)}{\tilde{V} \cdot \tilde{\nabla}_p (\zeta + f)} + \underset{(4)}{\omega \frac{\partial}{\partial p}(\zeta + f)} = \underset{(5)}{-(\zeta + f)\tilde{\nabla}_p \cdot \tilde{V}}$$

Term (2) is equal to zero because the Coriolis parameter does not change with time. Term (4) is dropped because this term is very small (Petterssen, 1956). If $\zeta = \overline{\zeta} + \zeta'$ and $\tilde{V} = \overline{\tilde{V}} + \tilde{V}'$, then by substitution into the expanded vorticity equation:

$$\underset{(1)}{\frac{\partial \overline{\zeta}}{\partial t}} + \underset{(2)}{\frac{\partial \zeta'}{\partial t}} + \underset{(3)}{\overline{\tilde{V}} \cdot \tilde{\nabla}_p (\overline{\zeta})} + \underset{(4)}{\overline{\tilde{V}} \cdot \tilde{\nabla}_p (\zeta' + f)} + \underset{(5)}{\tilde{V}' \cdot \tilde{\nabla}_p (\overline{\zeta})} + \underset{(6)}{\tilde{V}' \cdot \tilde{\nabla}_p (\zeta')}$$

$$\underset{0}{(1)} \quad \underset{2.10^{-9}s^{-2}}{(2)} \quad \underset{2.5x10^{-10}s^{-2}}{(3)} \quad \underset{2.5x10^{-9}s^{-2}}{(4)} \quad \underset{3x10^{-10}s^{-2}}{(5)} \quad \underset{10^{-10}s^{-2}}{(6)}$$

$$+ \underset{(7)}{\tilde{V}' \cdot \tilde{\nabla}_p (f)} = \underset{(8)}{-(\overline{\zeta} + \zeta' + f)\tilde{\nabla}_p \cdot \overline{\tilde{V}}} - \underset{(9)}{\overline{\zeta}\tilde{\nabla}_p \cdot \tilde{V}'} - \underset{(10)}{\zeta'\tilde{\nabla}_p \cdot \tilde{V}'} - \underset{(11)}{f\tilde{\nabla}_p \cdot \tilde{V}'}$$

$$\underset{7.5x10^{-11}s^{-2}}{(7)} \quad \underset{1x10^{-10}s^{-2}}{(8)} \quad \underset{3x10^{-10}s^{-2}}{(9)} \quad \underset{1x10^{-9}s^{-2}}{(10)} \quad \underset{3x10^{-9}s^{-2}}{(11)}$$

Typical values from this study are shown below their respective terms. Term (1) is equal to zero by the definition of a time mean. The dominant terms of this equation are

$$\frac{\partial \zeta'}{\partial t} + \bar{\tilde{V}} \cdot \tilde{\nabla}_p (\zeta' + f) = - (\zeta' + f) \tilde{\nabla}_p \cdot \tilde{V}' \qquad \text{(A1)}$$

The importance of the dropped marginal terms, terms (3), (5) and (9), vary somewhat along the track of the vortex, as is reflected in the aberrant divergence couplet on 12Z 28 June 1973 map (Figure 15b). Generally though, this equation does explain the presence of the divergence pattern found with the perturbation vortex.

As an example of the meaning of this equation, at upper levels where the winds move faster than the perturbation vorticity pattern, if an observer were upstream from the center of perturbation vorticity and moving with the flow, the local term $\frac{\partial \zeta'}{\partial t}$ would be negative and less than the positive advection term $(\tilde{V} \cdot \tilde{\nabla}_p (\zeta' + f))$, and convergence would be necessary to balance the equation. If the observer were downstream of the perturbation vorticity maximum, the local term would be positive and still less than the negative advection term, and divergence must take place (see Figure A-1). At lower levels where the flow is slower than the movement of the perturbation vorticity pattern, the local term would be greater than the advective term and the opposite divergences would be found.

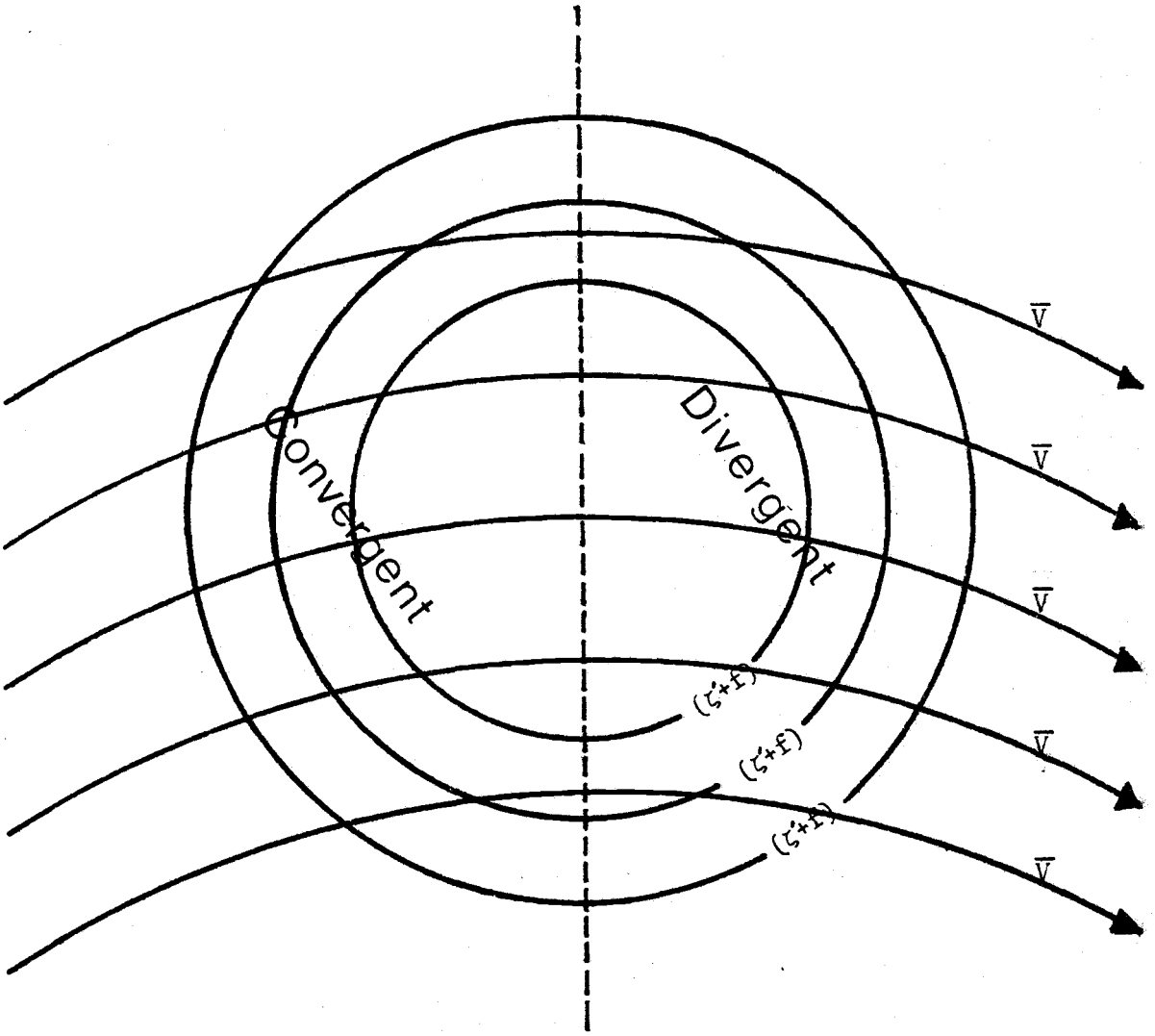

Figure A-1. Approximate 300mb convergent-divergent regions with respect to a perturbation vortex. Concentric isolines are absolute vorticity ($\zeta+f$), decreasing outward. Streamlines are of the mean wind ($\overline{V}$).